# Electronic structure calculations for point defects, interfaces, and nanostructures of $TiO_2$

Huynh Anh Huy

# Electronic structure calculations for point defects, interfaces, and nanostructures of $TiO_2$

(Berechnungen der elektronischen Struktur für Punktdefekte, Oberflächen, und Nanostrukturen von $TiO_2$)

von

Huynh Anh Huy

Dem Fachbereich für Physik und Elektrotechnik
der Universität Bremen
zur Erlangung des akademischen Grades eines
Doktors der Naturwissenschaften (Dr. rer. nat.)
genehmigte Dissertation

Tag der Einreichung: 31. Juli 2012
Tag der mündlichen Prüfung: 7. September 2012

Erstgutacher: Prof. Dr. rer. nat. Thomas Frauenheim
Zweitgutacher: Prof. Dr. rer. nat. Tim Wehling

# ACKNOWLEDGEMENTS

First and foremost, I would like to thank my supervisor, Professor Thomas Frauenheim, for providing me an excellent chance to work and to complete this PhD project at the Bremen Center for Computational Materials Science (BCCMS), University of Bremen. His patient and endless support was essentially important for me to complete this work.

My great appreciation goes to Professor Peter Deák for his tremendous support and help which are impossible to be overestimated. Without his encouragement and guidance, this thesis would not have materialized. I would like to thank Dr. Bálint Aradi for many technical discussions as well as helps for solving many programming problems. My special thank also goes to Professor Vu Ngoc Tuoc who introduced me to the BCCMS and exchanged his interesting ideas during my studying time here.

I would like to take this opportunity to thank the Training and Research Improvement Grant, University of Cantho for financially supporting me during this work. Also, I wish to express my sincere thank to the wonderful secretaries of the BCCMS and of the TRIG project who have willingly cared and helped me to solve all procedural problems between Cantho University and Bremen University.

I am grateful to all my friends in Bremen for being the surrogate family during the time I stayed in here. My thanks and appreciations also go to my colleagues and people who have willingly helped me out with their abilities.

Finally, I am forever indebted to my parents and my wife for their understanding, endless patience and encouragement in completing this project.

# TABLE OF CONTENTS

# LIST OF FIGURES

**Figure**

# LIST OF TABLES

**Table**

# ABSTRACT


**Electronic structure calculations for point defects, interfaces, and nanostructures of $TiO_2$**

Transparent conducting oxides (TCOs) play an important role not only in optoelectronic and photovoltaic devices but also in future transparent electronics. A transparent conductor arises upon degenerately doping a semiconductor (insulator) so that the conduction becomes metallic (resistivity $\sim$ temperature). The extra electrons occupy the conduction band (CB) states of the host and the conductivity is determined by the electron optical effective mass. Recently, anatase $TiO_2$ films doped with Nb, i.e., $Ti_{1-x}Nb_xO_2$ (TNO), have attracted a great deal of interest as a promising candidate for TCO applications because of their low resistivity ($\sim 2 \times 10^{-4}\Omega$cm) and high optical transmittance (90 % in the visible light region). A few experimental studies have been reported for the optical effective mass of electrons as a function of the carrier concentration in Nb-doped anatase, on the directions which are either orthogonal or parallel to the tetragonal axis of the crystal.

In this thesis, I have determined the optical effective mass of electrons in Nb-doped anatase based on band structure calculations. The anisotropy of the crystal and the nonparabolicity of the bands have both been taken into account. I have found that in the range concentration which is relevant to transparent conductive oxide applications, the optical effective mass is determined by several branches of the conduction band, leading to a complicated dependence on the carrier concentration. The function for the optical effective mass obtained by our calculations agrees well with that obtained experimentally. In particular, the strong anisotropy of the optical

effective mass has already been confirmed [1].

Although Ta-doping of anatase $TiO_2$ appears to be effective as well, this possibility has been not well explored. I have compared the two dopants, i.e., Nb and Ta, for doping anatase $TiO_2$. The Ta dopant has a considerably higher solubility and a lower optical effective mass, thus acquiring more advantages than Nb. Moreover, my calculations have also explained why a reducing atmosphere is necessary for the efficient dopant incorporation, without invoking oxygen vacancies as proposed in the literature. [2]

There is no study on the effects from the quantum confinement of dopants in anatase nanowires (ANWs). Therefore, I report here the first demonstration on the role of Nb- and Ta-dopants in ANWs. The pure ANWs cut by keeping the screw axis of the original bulk structures are consistently lower in energy than the similarly oriented nanowires in which the screw symmetry is destroyed. [3] Both Nb and Ta dopants prefer the sub-corner sites of the most stable ANWs. At the highest symmetry, the band structure of the doped ANW is similar to that of the perfect one. [4]

The increase of the photocatalytic activity upon mixing rutile and anatase powders is usually explained by assuming change separation between the two phases. There are many contradicting theories regarding the particular charge transfer between these phases. Therefore, another goal of this thesis is to study the electronic properties of the interface between anatase and rutile phases of $TiO_2$. By calculating the band line-up of a rutile-anatase interface, I have found that both the conduction band minimum (CBM) and the valence band maximum (VBM) of the rutile phase are higher than those of the anatase phase. As a result, electrons are expected to transfer from the rutile phase to the anatase phase while holes move in the opposite direction. [5]

In my work, the optical electron effective mass is determined from the band structure of the material, which is in turn calculated by the version of density functional

theory (DFT) in the generalized gradient approximation (GGA) implemented in the *Vienna Ab Initio Simulation Package* (VASP) package. For bulk materials, both the Perdew-Berke-Enzerhof (PBE) and the screened hybrid functional (HSE06) are used for the exchange energy. Although the HSE06 functional gives better results compared with the existing experimental measurements for Nb- and Ta-doped anatase $TiO_2$ bulk materials, similar calculations with HSE06 for nanowires are far more expensive. Therefore, my calculations for nanowires are carried out only with the pure GGA-PBE functional. To determine the rutile-anatase interface, I have used the density functional based tight binding (DFTB) method for the molecular dynamic simulations, and then relaxed by *ab initio* calculations with PBE functional at 0K.

# CHAPTER I

# Introduction

*Titanium dioxide $TiO_2$ has been widely used in industry for the last four decades, mainly as a white pigment, or for photocatalytic air- and water-purification. It has been recently found that $TiO_2$ can be used as a transparent conducting oxide (TCO) material. Because of the higher photocatalytic activity, mixtures of rutile and anatase $TiO_2$ have also attracted much attention. Moreover, $TiO_2$ can easily be nanostructured. In fact, nanowires with diameters of only $4-5\AA$ could be fabricated. In this Chaper, I provide some background which is needed for the work on $TiO_2$ presented throughout this thesis.*

## 1.1 TCO application of $TiO_2$

Optoelectronic and photovoltaic devices such as flat panel displays, light emitting diodes, or electrochemical solar cells, all require transparent electrodes [6, 7, 8, 9]. To be used in these devices, the transparent electrodes must have a resistivity of $10^{-3}\Omega$cm or less and an average transmittance above 80% in the visible range. This implies that the materials for the transparent electrodes should have a carrier concentration of the order of $10^{20}\text{cm}^{-3}$ or higher and a band gap above 3eV. Since the degenerately doped wide band gap oxides can achieve these requirements, such transparent conducting oxides (TCOs) can be used in the optoelectronic and photovoltaic devices.

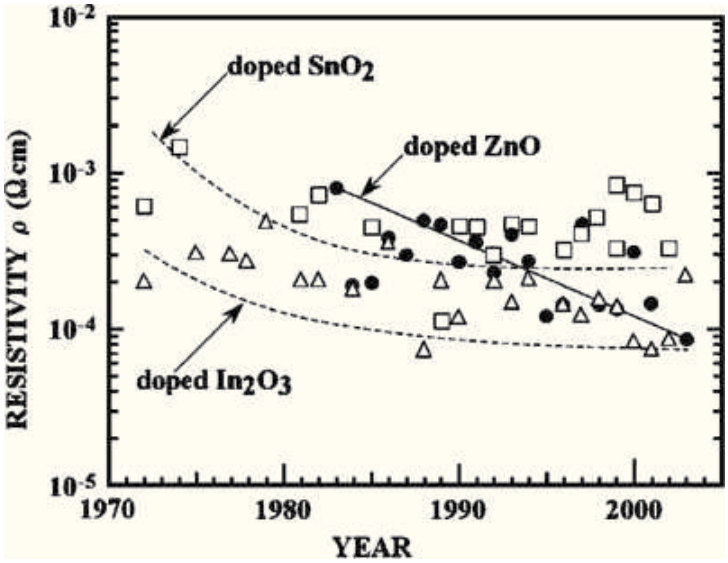


Figure 1.1: Reported resistivity of impurity-doped binary compound-based TCO films from 1972 - present. Squares, triangles, and circles are used for impurity-doped SnO2, In2O3, and ZnO, respectively. Reproduced from Ref. [13]

Most of the research activities in developing TCO thin films have been concentrated on various types of transition metal oxides [10]. Tin-doped $In_2O_3$ (ITO) is the most widely used TCO nowadays because of its excellent properties and ease of fabrication [11]. However, due to the high cost and the shortage of indium, new substitute materials are highly needed. Of the alternatives, $SnO_2$ doped with fluorine has typically an order of magnitude higher in the resistivity [7]. Much effort has also been spent on the development of TCOs based on ZnO because of its low resistivity [12]. On Figure 1.1, the minimum resistivity of TCO films reported during the last 40 years is shown, revealing that while the minimum resistivity of doped ZnO films is still decreasing, those of doped $SnO_2$ and $In_2O_3$ are essentially unchanged during the last 20 years [13].

Among the transition metal oxides, the ZnO film is more suitable for wide applications because of its low resistivity. However, it is much more difficult to control the oxidation of Zn in highly conductive and transparent ZnO TCO films because

Zn is highly chemically active in an oxidizing atmosphere. [14] Various sputtering techniques have been developed; however, the problem has not yet been completely resolved [15]. Consequently, it is highly desired to extend the variety of TCOs. Recently, Nb- or Ta-doped anatase $TiO_2$ has been reported to exhibit low resistivity ($2 \times 10^{-4}\Omega$cm at the room temperature) and high transmittance (95 % in the visible light region) in epitaxial [16, 17, 18, 19]. Motivated by these results, my thesis has concentrated on the electronic properties of $n$-type doped anatase $TiO_2$, the new promising TCO material which demonstrates extra advantages over ITO and ZnO to be used as a common antireflection coating and resistant to hydrogen-containing environments [20, 21].

In a degenerately $n$-type doped wide band gap semiconductor, the metallic conductivity can arise from a half-filled donor band which is created by the interaction between the impurities. It is often believed that this is the case of ITO although the defect band can overlap with the CB. In some cases, the defect band consists of effective-mass-like states, i.e. the extra electrons essentially fill CB states. While the ITO has an isotropic $s$-orbital-dominated conduction band, the case of anatase $TiO_2$ is more complicated. In particular, the conduction band of anatase $TiO_2$ is composed mainly by anisotropic Ti $3d$ orbitals. As I have observed, in Nb-doped anatase, these CB states are partially filled with electrons. Therefore, the balance between increasing carrier concentration and the carrier scattering by ionized donor, which play a role in determining the optimum conductivity, can also be influenced by the carrier concentration dependence of a concept called "optical effective mass".

The conventional effective mass is defined as the curvature, or the $2^{\text{nd}}$ derivative, of the dispersion curve. If the dispersion curve is ideally parabolic, i.e., there is no change in the curvature, the effective mass will be constant everywhere. Based on this simple assumption, recent theoretical calculations in Nb-doped anatase reported two values for the band-edge effective mass which is independent of the doping con-

centration. On the transverse direction which is orthogonal to the main axis, the effective mas is $m_{\perp} = 0.42m_0$ while on the longitudinal direction which is parallel to the main axis, $m_{\parallel} = 4.05m_0$ [22, 23]. In reality, because the actual CB of Nb-doped anatase is non-parabolic, the curvature has to depend on the $k$-wavevector. In addition, contributions from higher branches of the CB play a role in measuring the conductivity, as predicted in Refs. [22, 24, 25]. A new concept called "optical effective mass" is defined here to describe the non-parabolic CB, taking into account both the anisotropy of the crystal and the nonparabolicity of all the bands up to the Fermi level. By this definition, the carrier concentration is relevant to the concept of optical effective mass. From the literature, it has been indicated that the optical effective mass may be fairly different from, e.g., considerably bigger than, the band edge effective mass [26].

In consistence with the above discussion, measurements of the optical effective mass has indicated a strong dependence on the carrier concentration of the optical effective mass. Over the concentration range of $10^{20} - 10^{21}\text{cm}^{-3}$, the optical effective mass increases from $0.2m_0$ to $0.6m_0$ along the orthogonal direction and from $0.5m_0$ to $3.3m_0$ along the parallel direction[27, 28]. This increase can be interpreted as the consequence of the non-parabolicity of the lowest CB. In this thesis, I will show that higher branches of the CB play a significant role in the concentration dependence of the optical effective mass. Calculations for the optical effective mass of electrons as a function of the carrier concentration are based on band structure calculations which take into account both the anisotropy of the crystal and the non-parabolicity of the bands, for all bands up to the Fermi level, which is relevant to the given concentration [1].

Besides Nb-, Ta-doping of anatase $TiO_2$ has also been shown to be a viable candidate for replacing ITO as a transparent conductor oxide. Because Ta-doped anatase $TiO_2$ has been not well explored yet [29, 18, 30, 31, 32], a comparison on several as-

pects of these two dopants is given based on calculations for the electronic structures of Nb- and Ta-doped anatase. First, the optical effective masses on the orthogonal direction of Ta-doped anatase are found to be similar with that of Nb-doped one while on the parallel direction, the optical effective mass of Ta-doped anatase is about 60% of that of the Nb-doped anatase [2]. Second, because a high doping concentration is required for achieving metallic conduction in a TCO, a high solubility for a given dopant is an important criterion. For the dopant solubility, I have found that because Ta-substitution of a Ti-atom requires a considerably smaller energy than Nb-substitution does, Ta has definite advantages over Nb in doping anatase $TiO_2$ for TCO purposes. Finally, several experiments have shown that large dopant concentrations in anatase films can be achieved by applying a reducing atmosphere during growth [33, 22, 31]. By calculating the defect formation heat as a function of the oxygen chemical potential, a clear explanation is given in my thesis for the role of the reducing atmosphere on efficient dopant incorporation, without invoking oxygen vacancies as a factor in activating the dopant as proposed earlier in the literature [23].

## 1.2 $TiO_2$ nanowires and their doping by Nb and Ta

$TiO_2$ is widely studied because of its promising properties and a myriad of applications. The functionality of titania-based devices can be extended further on two directions: doping and size reduction to the nanoscale. For example, because of a very high specific surface area, nanostructures exhibit various advantages for photocatalysis and in electrochemical solar cells, where $TiO_2$ is used as an electron transmitter. While the first part of my thesis is devoted for the doping of $TiO_2$ from the viewpoint of TCO applications, the nanostructures of $TiO_2$ are considered in the second part of my thesis.

$TiO_2$ nanowires can easily be fabricated. Many methods have been used for the

synthesis of $TiO_2$ nanowires such as vapor phase deposition oxidation of Ti metal [34], solution chemistry synthesis [35], and template-assisted approach [36]. Recently, Liu and Yang have synthesized $TiO_2$ nanowires with diameters on the Angstrom scale, down to a diameter limit of about 4-5 Å.[37] This experimentally accessible size can also be easily considered by theoretical calculations.

Many interesting properties arise from the small sizes of the nanostructures. For example, the energy gap of the nanostructures is increased because of the quantum confinement effect. Because of the small sizes of the nanostructures, sites are not completely equivalent, so the doping sites also play a role, which will be addressed in my thesis.

Several structural properties of $TiO_2$ nanowires have been theoretically predicted. In Ref. [38], Zhang *et al.* studied the formation energy of $TiO_2$ wires built from $Ti_2O_4$ blocks with tetrahedral coordination of the Ti atoms. They found that the size and the shape of $TiO_2$ nanowires have important effects on their structural stability and the energy gap. Iacomino *et al.* [39] investigated the structures and electronic properties of anatase wires with different orientations and various surface terminations as a function of diameter.

A bare $TiO_2$ nanowire of a variety of diameters can be built by cutting the respective bulk crystal along a chosen direction. The choice of the central axis and the cutting-planes determines the structure and electronic properties of the nanowire. In Iacomino's calculation, the [001]-oriented anatase nanowires were cut along a central axis passing through Ti atoms, resulting in the mirror symmetry but no screw axis in the wires. However, because Ångstrom-scaled $TiO_2$ nanowires consist of a few atomic layers, even a small difference in their geometries can have a significant impact on their stability or the electronic properties. Recently, Aradi *et al.* [3] have investigated the relative stability of [001] nanowires with the central axes going through a Ti atom (with 2-fold axis) and through the interstitial site (with screw axis). It was found

that the nanowires cut by keeping the screw axis of the original bulk structure are consistently lower in energy both in rutile and anatase than in the similar oriented nanowires in which this symmetry is destroyed. It has been also shown that the direct or indirect nature of the $TiO_2$ wire's band gap is coupled to the absence or presence of the screw axis.

There is as yet no study about the effect of quantum confinement of doping in anatase nanowires. Therefore, my thesis aims to report the first demonstration of the role of both Nb- and Ta-dopants in anatase nanowires. Taking into account the role of symmetry, I have investigated the influence of dopants on the structural and electronic properties of nanowires. Both Nb and Ta dopants prefer the full-coordinated Ti sites. If the screw symmetry of the doped anatase nanowire is kept, its band structure is similar to that of the perfect one. [4]

## 1.3 Charge transfer and the photocatalytic applications of $TiO_2$

Since Fujishima and Honda [40] published a paper on the photocatalytic water splitting by $TiO_2$, there have been a large amount of investigations regarding to the photocatalytic applications of this material. $TiO_2$ was found to be very effective in decomposing various carbon based on molecules through redox reaction under illumination by near ultraviolet (above band gap) light. The illumination produces electron-hole pairs. One of these can catalyse reactions on the surface, while the other gets trapped in the bulk scavenged by adsorbates or molecules in the environment.

There are many methods to increase the efficiency of the photocatalytic application, which depends on the light absorption and on the recombination rate of electron and holes. One of the methods is to shift the light absorption threshold into the visible region by doping. Asahi [41] has published the first such paper using nitrogen

doped $TiO_2$. Another way is the incorporation of metal nanoparticles such as silver or gold into the $TiO_2$ [42]. Because silver has the Fermi level below the conduction band of $TiO_2$, the photoexited electron from the conduction band can be effectively trapped by silver, so the hole can react the surface and catalyse surface reactions. Yet another strategy is the use of mixed powders of anatase and rutile. The charge separation between the two phases was proposed to explain the increased catalytic activity. In fact, due to the different band gaps, the band offsets between anatase and rutile can see charge transfer across the interface, decreasing the recombination electrons and holes.

Over the years, a number of experimental papers were given, predicting different band offsets between anatase and rutile. The first model came from Gesenhues with the suggestion of hole accumulation in rutile, based on the assumed alignment of the valence bands [43]. Using the XPS technique, in contrast, Bickley *et al.* [44] suggested the so-called "rutile sink" model for the electrons assuming that the conduction band edge of rutile being lower in energy than that of anatase. This model was also supported by the work of Kho *et al.* [45].

In another study, by measuring the ERP spectra under visible illumination, Hurum *et al.* [46, 47] established the existence of electron trapping sites which is 0.8 eV below the conduction band edge of anatase. Nakajima *et al.* [48] measured the band gap of $TiO_2$ powder with various rutile phase by photoluminescence excitation (PLE) spectroscopy. They found that electrons transfer from the higher conduction band of anatase to the lower one of rutile. Therefore, the recombination of electrons and holes in rutile is stronger than in anatase phase.

Recently, based on experimental investigations under both UV and visible light irradiation, Nair *et al.* [49] suggested a model for explaining the mechanism for photoactivity of the mixed phase, and supported the "rutile sink". This is also corroborated by an observation of Scotti *et al.* [50] based on EPR measurements, where

in the presence of a large number of electrons has been reported on the rutile side of the interface. Under the visible light, the radiation is absorbed by rutile phase only, resulting in excited electrons in its conduction band, these electrons will move to the anatase conduction band.

As discussed, there are many conflicting experimental reports on the charge transfer mechanism while knowledge of the relative position of the conduction band edges is the key to understand charge transfer process. Recently, Deak *et al.* [51] have calculated the band offset of the bulk crystals between anatase and rutile aligning the branching point energy (BPE) (or change neutrality level) [52]. They found that the CB of rutile lies higher than that of anatase by about $0.3 - 0.4$eV. This can, however, be influenced by the interface between the actual anatase and the rutile. Therefore, the last aim of this thesis is to investigate the role of interface on the band line-ups and on the mechanism of charge transfer. I have found that both the conduction band minimum (CBM) and the valence band maximum (VBM) of the rutile phase are higher than those of anatase. As a result, electrons are transfered from the rutile phase to the anatase phase, while holes move in the opposite direction. [5]

## 1.4 Organization of the manuscript

This thesis is organized in six Chapters. In Chapter 2, I present a brief overview of the computational methods used in this work, which is the density functional theory (DFT) with GGA-PBE and HSE06 functionals for the exchange and correlation energies. Brief introductions on the DFTB method and the VASP simulation packages used for calculations are also discussed in this Chapter. Some background for calculations of the optical effective mass is also introduced.

The main results are exposed in three subsequent Chapters. Chapter 3 is started with the investigations on the band structures of pure and Nb-doped anatase $TiO_2$. The optical effective masses are calculated in both the orthogonal and the parallel

directions by fitting a polynomial expression to the calculated dispersion relation. For obtaining the optical effective mass up to the high Fermi level positions in the CB, the accuracy of the band structure is critical. Local and semilocal approximations of the DFT (like GGA) are known to underestimate, not only the gap but also the width of the bands. Therefore, in this chapter, I use the screened hybrid functional HSE06 which provides the electronic structure of $TiO_2$ in the excellent agreement with experiment. In the second part of this Chapter, I discuss the formation energy of Nb and Ta dopants on and the values of optical effective mass, and show that Ta dopant is a better alternative material than Nb dopant.

In Chapter 4, I review a recent study of the bare $TiO_2$ nanowires cut from their respective bulk crystals along [001] direction. Then, I discuss the favoured sites of dopants and the role of symmetry in the band structure of these nanowires. In nanowire studying, I only carry out the PBE calculations because HSE06 ones are too expensive .

In Chapter 5, I deal with the particular interface between anatase and rutile. The interface model is created by DFTB-MD, and the alignment of the average electrostatic potential is calculated with DFT-PBE methods. The result is used to determine the alignment of the HSE06 electronic structures.

Finally, in Chapter 6, I summarize the results so far and outline the directions for future work in this field.

# CHAPTER II

# Theoretical Methods

*Nowadays, density functional theory (DFT) is a standard toolkit to study electronic properties of materials. The aim of this Chapter is to present this approach for describing the ground state properties. This Chapter also introduces some approximations for the exchange-corelation functional. In addition, a brief description of the self-consistent charge density-functional-based tight-binding (SCC-DFTB) approach is given. At the end of Chapter, the method for calculating optical effective mass is illustrated.*

## 2.1 The many-electron problem

To describe the stationary state of a system, in quantum mechanics, we solve the time-independent Schrödinger equation for the wave function $\Psi$

$$\hat{H}\Psi = E\Psi. \tag{2.1}$$

Here, the Hamiltonian operator within the Born-Openheimer approximation (fixed positions of the nuclei) is [53]

$$\hat{H} = \hat{T} + \hat{V}_{\text{int}} + \hat{V}_{\text{ext}} + \hat{V}_{\text{II}}, \tag{2.2}$$

where $\hat{T}$ is the kinetic energy of electrons, $\hat{V}_{\text{int}}$, $\hat{V}_{\text{II}}$ are the electron - electron, nuclei - nuclei interactions, respectively, and $\hat{V}_{\text{ext}}$ is the potential of nuclei acting on the electrons.

The total energy of the system $E$ can be determined by the expectation value of the Hamiltonian,

$$E = \frac{\langle\psi|\hat{H}|\psi\rangle}{\langle\psi|\psi\rangle} = \langle\hat{H}\rangle = \langle\hat{T}\rangle + \langle\hat{V}_{\text{int}}\rangle + \int d\mathbf{r}\hat{V}_{\text{ext}}\rho(\mathbf{r}) + \langle\hat{V}_{\text{II}}\rangle, \tag{2.3}$$

where $\rho(\mathbf{r}) = \int d\mathbf{r}|\Psi(\mathbf{r})|^2$ is the density of states (DOS).

To know the electronic properties, we need to solve the Schrödinger equation (2.1). However, this equation is impossible to solve exactly because of the large number of variables. For instance, even one $TiO_2$ molecule has 38 electrons, so equation (2.1) is a partial differential equation of 114 spatial coordinates. Therefore, approximation methods can be used. The two most common techniques to reduce the many-electron problem are the Hartree-Fock (HF) theory and the density functional theory (DFT). The former considers the total energy as a functional of the many-body wave function, constructed from independent single-particle states as a single Slater determinant. The single-particle states fulfill the Pauli principle, but are not correlated. The latter considers the total energy as a functional of the electron density. In the last two decades, the DFT has been most often used because of its higher efficiency.

## 2.2 Hohenberg-Kohn theorems

The basis idea of DFT is that any properties of a many body system can be described by a functional of ground state. A complicated of many body wave function can be replaced by the electron density $\rho(\mathbf{r})$:

$$\rho(\mathbf{r}_1) = N \int |\Psi(\mathbf{r}_1, \mathbf{r}_2, ..., \mathbf{r}_N)|^2 d\mathbf{r}_2 ... d\mathbf{r}_N \tag{2.4}$$

The formulation of DFT is based on the Hohenberg and Kohn theorems as follow [54]

*Theorem 1: "For any system of electrons in an external potential $V_{ext}$, that potential is determined uniquely, except for a constant, by the ground state density $\rho(\mathbf{r})$."*

The many body wave-function can be replaced by the electron charge density $\rho(\mathbf{r})$ within the external potential $V_{\text{ext}}$. Therefore, the total energy can be represented as a function of the electronic density $E[\rho(\mathbf{r})]$.

*Theorem 2: "A universal functional $F[\rho(\mathbf{r})]$ for the energy of density $E[\rho(\mathbf{r})]$ can be defined for all electron systems. The exact ground state energy is the global minimum for a given $V_{ext}$, and the density $\rho(\mathbf{r})$ which minimizes this functional is the exact ground state density $\rho(\mathbf{r})$."*

If the universal functional $F[\rho(\mathbf{r})] = T[\rho(\mathbf{r})] + V_{\text{int}}[\rho(\mathbf{r})]$ is known, by minimizing the total energy of the system under the constraint $\int \rho(\mathbf{r})d\mathbf{r} = N$, we will find the exact ground state energy

$$E = min\Big\{F[\rho(\mathbf{r})] + \int \rho(\mathbf{r})V_{\text{ext}}d\mathbf{r} + V_{\text{II}}\Big\}. \tag{2.5}$$

The Hohenberg-Kohn theorems prove that the exact ground state energy can be found from the functional $F[\rho]$ but they do not describe in detail about the construction of this functional.

## 2.3 Kohn-Sham equation

In order to construct the $F[\rho(\mathbf{r})]$ functional, Kohn and Sham have introduced the following "Ansatz" [55]

*"The ground state density of the original interacting system is equal to that of some chosen non-interacting system that is exactly soluble, with all difficult part (exchange and correlation) included in some approximate functional of the density."*

The exact ground state density $\rho(\mathbf{r})$ can be represented by the ground state density of an auxiliary system $\rho_{\mathrm{KS}}(\mathbf{r})$ of non-interacting particles given by

$$\rho_{\mathrm{KS}}(\mathbf{r}) = \sum_{i=1}^{N} |\Psi_i(\mathbf{r})|^2 \tag{2.6}$$

The auxiliary Hamiltonian contains a kinetic energy term and a local effective potential acting on electrons

$$H_{\mathrm{KS}}(\mathbf{r}) = -\frac{1}{2}\nabla^2 + V_{\mathrm{KS}}(\mathbf{r}). \tag{2.7}$$

The ground state energy functional in the Kohn Sham approach to the full interacting many-body problem is rewritten in the form

$$E_{\mathrm{KS}}[\rho(\mathbf{r})] = T_{\mathrm{s}}[\rho(\mathbf{r})] + E_{\mathrm{ext}}[\rho(\mathbf{r})] + E_{\mathrm{Hatree}}[\rho(\mathbf{r})] + E_{\mathrm{II}} + E_{\mathrm{xc}}[\rho(\mathbf{r})], \tag{2.8}$$

with $E_{\mathrm{ext}}[\rho(\mathbf{r})] = \int \rho(\mathbf{r}) V_{\mathrm{ext}}(\mathbf{r}) d\mathbf{r}$.

Applying the variational principle for equation (2.8) and Lagrange multipliers method with the orthogonalization constraint, we get the Kohn-Sham equation for the single-particles

$$\Big[ -\frac{1}{2}\nabla^2 + V_{\mathrm{KS}}(\mathbf{r}) \Big] \psi_i(\mathbf{r}) = \epsilon_i \psi_i(\mathbf{r}), \tag{2.9}$$

with

$$V_{\mathrm{KS}}(\mathbf{r}) = V_{\mathrm{ext}}(\mathbf{r}) + \frac{\delta E_{\mathrm{Hartree}}[\rho(\mathbf{r})]}{\delta \rho(\mathbf{r})} + \frac{\delta E_{\mathrm{xc}}[\rho(\mathbf{r})]}{\delta \rho(\mathbf{r})} = V_{\mathrm{ext}}(\mathbf{r}) + V_{\mathrm{Hartree}}(\mathbf{r}) + V_{\mathrm{xc}}(\mathbf{r}). \tag{2.10}$$

By solving self-consistently the Kohn-Sham equations for independent particles (2.9), we can find the exact ground state energy and density of the many body problem. However, the last term exchange-correlation potential $V_{\mathrm{xc}}(\mathbf{r})$ in equation (2.10) and its corresponding energy expression $E_{\mathrm{xc}}[\rho(\mathbf{r})]$ are unknown.

## 2.4 Functionals for exchange and correlation

### 2.4.1 Local density approximation (LDA)

The simplest approximation for the exchange and correlation is to assume that the density can be treated locally as a uniform electron gas.

$$E_{\rm xc}^{\rm LDA}[\rho(\mathbf{r})] = \int \rho(\mathbf{r})\epsilon_{\rm xc}[\rho(\mathbf{r})]d\mathbf{r}, \tag{2.11}$$

where $\rho(\mathbf{r})$ is the electron density, and $\epsilon_{\rm xc}[\rho(\mathbf{r})]$ is the exchange and correlation density.

The exchange-corelation potential is given [56]

$$V_{\rm xc}^{\rm LDA}[\rho(\mathbf{r})] = \frac{\delta E_{\rm xc}^{\rm LDA}[\rho(\mathbf{r})]}{\delta\rho(\mathbf{r})} = \epsilon_{\rm xc}[\rho(\mathbf{r})] + \rho(\mathbf{r})\frac{\partial\epsilon[\rho(\mathbf{r})]}{\partial\rho(\mathbf{r})}. \tag{2.12}$$

### 2.4.2 Generalized gradient approximations (GGAs)

In the generalized gradient approximations (GGAs), the exchange-correlation energy depends not only on the density but also on its gradient [57]

$$E_{\rm xc}^{\rm GGA} = \int d\mathbf{r}\rho(\mathbf{r})e_{\rm xc}[\rho(\mathbf{r}), \nabla\rho(\mathbf{r}), ...] = \int d\mathbf{r}\rho(\mathbf{r})\epsilon_{\rm xc}^{\rm hom}[\rho(\mathbf{r})]F_{\rm xc}[\rho(\mathbf{r}), \nabla\rho(\mathbf{r}), ...]. \tag{2.13}$$

The exchange energy is well established [58]; however the best choice for $F_{\rm xc}$ is still debated. The most commonly $F_{\rm xc}$ forms were suggested by Becke(B88) [59], Perdew and Wang (PW91) [58], and Perdew, Burke, and Enzerhof (PBE) [60].

### 2.4.3 LDA/GGA problems

Despite the successes with standard local and semi-local approximations for the exchange functional in DFT, there are serious limitations especially for a quantitative description the electronic structure of the strongly correlated systems of d(f)-

electrons. [61] The LDA/GGA functionals underestimate not only the band gap but also the width of the valence and conduction bands. [62]. For example, both LDA and GGA predicted the quasi particle band gap of anatase $TiO_2$ to be 2.14eV at 0K compared with the experimental optical band gap of 3.4eV [63]. The other error is their inability of predicting localized states in doped semiconductors. These calculations predicted Nb- and Ta-dop rutile $TiO_2$ to be metal, in contrast to the experimental observation of a semiconductor with a localized gap state. [64]

Several reasons have been proposed to explain LDA/GGA failure. Recently, Lany and Zunger [65] have suggested the incorrect behavior of the total energy as a function of the occupation numbers $E(n)$. The exact function should be linear, however, in LDA/GGA, the energy is the convex function resulting small band gap and delocalized dopant states.

One way to overcome the deficiency of ordinary LDA and GGA in case of the d-state is adding a Hubbard-U term to the energy functional [66]

$$E_{\mathrm{LDA+U}} = E_{\mathrm{LDA}} + \sum_m \frac{U_m - J_m}{2}\Big(\sum_\sigma n_{m,\sigma} - n_{m,\sigma}^2\Big), \tag{2.14}$$

where $n_{m,\sigma}$ is the occupation number of the $\mathrm{m}^{\mathrm{th}}$ $d$ state, U reflects the strength of Coulomb interaction between $d$ electrons, and the parameter J adjusts the strength of the exchange interaction.

This method gave a good qualitative agreement with the experimental data on Nb-doped rutile $TiO_2$, resulting in a localized gap state, corresponding to a small polaron on a single Ti site [64]. However, at the same time, doped anatase $TiO_2$ did not show metallic behavior, because the on-site Coulomb correction gave rise to a localized defect state in that case. [67]. Besides, the value of the Hubbard-U parameter cannot be determined in a general way, changing the U will change the electronic properties. [64] It is, therefore, necessary to find a better method to

overcome these problems.

### 2.4.4 The hybrid functional screened HSE06

One widely used way to overcome the standard DFT problems is to mix Hartree-Fock (HF) exchange potential into LDA/GGA functional. It is shown that GGA exchange gives a convex approximation to $E(n)$ while HF is concave. Therefore, the combination of them may gives the correct behavior of linear $E(n)$. For example, the PBE0 hybrid functional [57] based on the PBE functional by Perdew *et al.* [60] is mixed with Hartree Fork exchange potential in a ratio $a = 1/4$

$$E_{\mathrm{xc}}^{\mathrm{PBE0}} = aE_{\mathrm{x}}^{\mathrm{HF}} + (1-a)E_{\mathrm{x}}^{\mathrm{PBE}} + E_{\mathrm{c}}^{\mathrm{PBE}} \tag{2.15}$$

In $TiO_2$, the PBE0 hybrid functional improves the gap of 3.2 eV but the energy function of the continuous occupation number is still a concave function. As a result, the energy eigenvalue decreases upon electron addition. A screening HF exchange is needed. In the Heyd-Scuseria-Ernzerhof hybrid functional (HSE06), [68, 69] the effect of screening is added to PBE0 with the screening length of 0.2 1/Å.

By using the HSE06 in $TiO_2$, Deák *et al.* has recently shown the better lattice constants and band structure (reproducing the band gap, changing the width of the conduction band and valence band) than Perdew-Burke-Ernzerhof (PBE) approach.[70] Because HSE06 corrects the linear E(n), a proper description of defect is shown exactly. For example, HSE06 predicted exactly the polaronic states occurring in rutile while Nb and Ta on Ti site rising to a shallow effective mass like (EMT) donor state. [70, 32] Therefore, the HSE06 method is employed to calculate the electronic properties of the Nb- and Ta-doping in anatase, as reported in Chapter 3.

## 2.5 Projector augmented waves (PAWs)

As I mentioned above, to investigate the electronic properties of materials, we solve the Kohn Sham wavefunctions in equation (2.9) by self-consistent method. The first important thing is to set a trial wavefunction $\Psi_{\mathbf{k}}(\mathbf{r})$. In a periodic system, the good initial wavefunction performed plane wave (PW) is a good solution because it is simple, unbiased, independent of atomic positions.

$$\Psi_{\mathbf{k}}(\mathbf{r}) = \frac{1}{\sqrt{\Omega}} \sum_{G} \tilde{u}_{\mathbf{k}} e^{(\mathbf{k}+\mathbf{G})\mathbf{r}} \tag{2.16}$$

where $\Omega$ denotes the volume of a unit cell, $\tilde{u}_{\mathbf{k}}$ is a parameter of Fourier expanding of Bloch function $u_{\mathbf{k}}$.

However, the convergence in description of the atomic core area is low because of very varying wavefunctions. Several methods have been developed to reduce not only the basic set size and but also the number of electrons, which are necessary for simplification. The most widely used method is based on two approximations: (i) the core electrons are frozen, only valence electrons define the electronic properties, (ii) the interaction between core and valence electrons can be modeled by a pseudopotential (PP) [71, 72].

The disadvantage of the pseudopotential is the incapability of restoring the true (full all electrons) wave function. To keep the true wave function $\Psi_v$ of valence electrons, the projector-augmented wave (PAW) method is suggested [73, 74]. This approach is a generalization of the pseudopotential and linear-augmented-plane-wave (LAPW). [75] In the PAW methods, the true wave function and the pseudo wave function $\tilde{\Psi}_v$ outside the core region (augmentation region) are related by the linear transformation $\hat{T}$

$$|\Psi_v\rangle = \hat{T}|\tilde{\Psi}_v\rangle. \tag{2.17}$$

The transformation operator is given by

$$\hat{T} = 1 + \sum_{\mathbf{R}} \hat{T}_{\mathbf{R}}, \tag{2.18}$$

where local contribution $\hat{T}_{\mathbf{R}}$ acts only on the atom site $\mathbf{R}$

$$\hat{T}_{\mathbf{R}}|\tilde{\Phi}_v\rangle = |\Phi_v\rangle - |\tilde{\Phi}_v\rangle. \tag{2.19}$$

Note that the true partial wave function $\Phi_v$ is equal to the pseudo partial wave-function $\tilde{\Phi}_v$ outside core radius $r_c$. Because transformation $\hat{T}$ is linear, the true wave function can be obtained from the pseudo wave function by

$$|\Psi_v\rangle = |\tilde{\Psi}_v\rangle + \sum_i (|\Phi_v\rangle - |\tilde{\Phi}_v\rangle)\langle\tilde{p}_i|\tilde{\Psi}_v\rangle, \tag{2.20}$$

here the projector function $\tilde{p}_i$ satisfies $\langle\tilde{p}_i|\tilde{\Psi}_v\rangle = \delta_{iv}$.

The charge density $\rho(\mathbf{r})$ is given by three contributions

$$\rho(\mathbf{r}) = \tilde{\rho}(\mathbf{r}) + \rho^1(\mathbf{r}) - \tilde{\rho}^1(\mathbf{r}) \tag{2.21}$$

Here, the first term is the pseudo charge density outside the core region (augmentation region) corresponding to $\tilde{\Psi}_v$, the last two terms are charge densities inside the augmentation region $\Phi_v$, and the rest one $\tilde{\Phi}_v$ (for detailed, see Ref. [73])

In my works, I used the Vienna ab-initio simulation package (VASP) [76, 77, 74, 78] because it allows to perform efficient DFT calculations for complex molecular systems like $TiO_2$. The PAW in VASP gives a good description because of smaller radius cut-off reconstruction, and more exact valence wavefunction with all nodes in the core region. The energy cut-off of $TiO_2$ is set to 420eV for the wave function and to 840eV for the charge density.

## 2.6 The density-functional-based tight-binding (DFTB) method

Another approach to determine the electronic structure and electronic properties of $TiO_2$ is to use a self-consistent charge density-functional-based tight-binding (SCC-DFTB) method. This method is based on the second-order expansion of the Kohn-Sham total energy of initial charge density $n_0$ and its small fluctuation $\delta n$[79, 80].

$$E = \Big[\sum_{i}^{\text{occ}} \langle \Psi_i | \hat{H}^0 | \Psi_i \rangle \Big] + \Big[ -\frac{1}{2} \int\int^{'} \frac{n_0 n_0^{'}}{|r - r'|} + E_{\text{xc}}[n_0] - \int V_{\text{xc}}[n_0] n_0 + E_{\text{ii}} \Big] + \Big[ \frac{1}{2} \int\int^{'} \Big( \frac{1}{|r - r'|} + \frac{\delta^2 E_{\text{xc}}}{\delta n \delta n'} \Big|_{n_0} \Big) \delta n \delta n' \Big],$$

where the first term $E_{\text{BS}}$ is the band structure energy, the second term $E_{\text{rep}}$ is a short-range repulsive two-particle interaction. The last term is the electrostatic interaction accounting for charge fluctuations. At larger distances, this term is neglected, we can replace by a simple pair-wise potential

$$\frac{1}{2} \int\int^{'} \Big( \frac{1}{|r - r'|} + \frac{\delta^2 E_{\text{xc}}}{\delta n \delta n'} \Big|_{n_0} \Big) \delta n \delta n' = \frac{1}{2} \sum_{\alpha\beta} \gamma_{\alpha\beta}(R_{\alpha\beta}) \Delta q_\alpha \Delta q_\beta, \tag{2.22}$$

where $\gamma_{\alpha\beta}(R_{\alpha\beta})$ is determined by Coulomb interaction of two pherical charge distributions centered in the atom $\alpha$ and $\beta$; $\Delta q_\alpha$ and $\Delta q_\beta$ are atomic charge fluctuations.

The wave function is expanded to a linear combination of atomic orbitals (LCAO) for valence electrons

$$\Psi^i(\mathbf{r}) = \sum_{\nu} c_\nu^i \phi_\nu(\mathbf{r} - \mathbf{R}_\alpha) \tag{2.23}$$

Applying the two-particle approximation, the nonzero Hamiltonian $H^0$ can be expressed

$$H^0_{\mu\nu} = \begin{cases} \varepsilon^\alpha_\mu, & \text{if } \alpha = \beta,\ \mu = \nu \\ \langle \phi^\alpha_\mu | \hat{T} + V^{\alpha,\beta}_{\text{KS}} | \phi^\beta_u \rangle, & \text{otherwise} \end{cases}, \tag{2.24}$$

where $V_{\mathrm{KS}}^{\alpha,\beta}$ stand for a pair effective potential operating only on the electrons in the atoms $\alpha$ and $\beta$.

Applying variation principle, we have a SCC-DFTB secular equation

$$\sum_{\nu} c_{\nu}^{\mathrm{KS}}(H_{\mu\nu}^{0} - \varepsilon_{\mathrm{KS}} S_{\mu\nu}) = 0 \tag{2.25}$$

where $S_{\mu\nu} = \langle \phi_{\alpha} | \phi_{\beta} \rangle$ represents the overlap between local speudoatomic orbitals.

Introducing a distance-dependent pairwise repulsive potential $V_{\mathrm{rep}}^{\alpha\beta}(R_{\alpha\beta})$, we can rewrite the total energy

$$E = \sum_{\mu\nu} c_{\mu}^{\mathrm{KS}*} c_{\nu}^{\mathrm{KS}} H_{\mu\nu}^{0} + \sum_{\alpha<\beta} V_{\mathrm{rep}}^{\alpha\beta}(R_{\alpha\beta}) + \frac{1}{2} \sum_{\alpha\beta} \gamma_{\alpha\beta}(R_{\alpha\beta}) \Delta q_{\alpha} \Delta q_{\beta} \tag{2.26}$$

Solving the equation (2.25), we determine eigenstates $c_{\nu}^{\mathrm{KS}}$ and then the first term in equation (2.26). The second term can be found by empirically fitting $E_{\mathrm{Elec}}^{\mathrm{DFTB}}$ to the corresponding total energy $E_{\mathrm{Elec}}^{\mathrm{DFT}}$. The last term describes the role of charge transfer, the atomic charges are determined self-consistently. The SCC-DFTB calculations were performed in DFTB+ code [81]. The precomputed matrix elements are held in Slater-Koster files.

## 2.7 Optical Effective Mass

Conductivity of a non-degenerate semiconductor

$$\sigma = \frac{n_e e^2 \tau(\varepsilon_{\mathrm{F}})}{m^{\star}} \tag{2.27}$$

where $n_e$ is electron concentration, $\tau$ is relaxation time and $m^{\star}$ is the effective mass given by [82]

$$\frac{1}{m^{\star}} = \frac{1}{\hbar^2} \frac{\partial^2 \varepsilon(\mathbf{k})}{\partial \mathbf{k}^2} \tag{2.28}$$

where $\varepsilon(\mathbf{k})$ is carrier energy function and $\mathbf{k}$ is wave vector in a periodic potential field.

In case of antisotropic band, the effective mass can be theoretically represented as a tensor with nine components $m^{\star}_{\mathrm{ij}}$

$$\frac{1}{m^{\star}_{\mathrm{ij}}} = \frac{1}{\hbar^2}\frac{\partial^2\varepsilon(\mathbf{k})}{\partial\mathbf{k}_i\partial\mathbf{k}_{\mathrm{j}}} \tag{2.29}$$

In an appropriately chosen coordinate system $m^{\star}$ becomes diagonal:

$$\frac{1}{m^{\star}} = \begin{pmatrix} \dfrac{1}{m_{xx}} & 0 & 0 \\ 0 & \dfrac{1}{m_{yy}} & 0 \\ 0 & 0 & \dfrac{1}{m_{zz}} \end{pmatrix} \tag{2.30}$$

In anatase $TiO_2$, we have $m_{xx} = m_{yy} = m_{\perp}$ and $m_{zz} = m_{\parallel}$ in orthorgonal and parallel to the main axis, respectively.

In non-degenerated n-type semiconductors, only the CBM is occupied at $kT$. In the vicinity of the CBM the $\varepsilon(\mathbf{k})$ can be approximated parabolically

$$\varepsilon(\mathbf{k}) = \sum_i \frac{\hbar^2 k_i^2}{2m^{\star}_{ii}} = \frac{\hbar^2 k_x^2}{2m^{\star}_{xx}} + \frac{\hbar^2 k_y^2}{2m^{\star}_{yy}} + \frac{\hbar^2 k_z^2}{2m^{\star}_{zz}} \tag{2.31}$$

with a constant $m^{\star}_{ii}$

For very high dopant concentrations, the parabolic approximation cannot be applied and $m^{\star}_{ii}(k)$ become k-dependent. In the isotropic relaxation time approximation, the conductivity becomes

$$\sigma = e^2 \int \frac{d\mathbf{k}}{4\pi^3}\mathbf{v}_{\mathbf{k}}\mathbf{v}_{\mathbf{k}}\tau(\varepsilon(\mathbf{k}))\Big(-\frac{\partial f_0}{\partial\varepsilon(\mathbf{k})}\Big), \tag{2.32}$$

where the velocity of electron $\mathbf{v}_{\mathbf{k}} = -\dfrac{1}{\hbar}\dfrac{\partial\varepsilon(\mathbf{k})}{\partial\mathbf{k}}$ and $f_0$ is the Fermi-Dirac distribution

in equilibrium. In a metal, the Fermi energy $\varepsilon_F$ is in the CB, and at low temperature

$$-\frac{\partial f_0}{\partial \varepsilon(\mathbf{k})} = \delta(\varepsilon(\mathbf{k}) - \varepsilon_F), \tag{2.33}$$

Taking this into account and decomposing the volume integral in the k-space into an energy integral and surface integral along equi-enegetic surface one obtains

$$\sigma = \frac{e^2\tau(\varepsilon_F)}{4\pi^3\hbar^2} \int\limits_{S(\varepsilon_\mathrm{F})} \mathbf{v}_\mathbf{k} d\mathbf{S} \tag{2.34}$$

This can be written to resemble the case of the semiconductor in equation (2.32), by introducing the so-called optical effective mass:

$$\frac{1}{m^\mathrm{opt}} = \frac{1}{4\pi^3\hbar^2 n_e} \int\limits_{S(\varepsilon_\mathrm{F})} \mathbf{v}_\mathbf{k} d\mathbf{S} \tag{2.35}$$

with

$$n_e = \frac{1}{4\pi^3} \int d\mathbf{k} \tag{2.36}$$

The name optical effective mass comes from the fact that its value is a function of the carrier concentration $n_e$ because of non-parabolic nature of the energy bands. If $\varepsilon_\mathrm{F}$ is high enough, several branches of the CB are occupied, then

$$\frac{1}{m^\mathrm{opt}} = \frac{1}{4\pi^3\hbar^2 n_e} \sum_\ell \int\limits_{S^\ell(\varepsilon_\mathrm{F})} \mathbf{v}^\ell_\mathbf{k} d\mathbf{S}^\ell \tag{2.37}$$

If the Fermi surface $S(\varepsilon^\ell_\mathrm{F})$ is continuous, the Gauss theory can be applied and

$$\frac{1}{m^\mathrm{opt}} = \frac{1}{4\pi^3\hbar^2 n_e} \sum_\ell \int\limits_{V^\ell(\varepsilon_\mathrm{F})} \Delta\varepsilon^\ell(\mathbf{k}) dV^\ell \tag{2.38}$$

where $V^\ell(\varepsilon_\mathrm{F})$ is a volume inside Fermi surface $S^\ell_{\varepsilon_\mathrm{F}}$

Here, I have summarized some approaches in DFT theory into $TiO_2$ material. The HSE06 approximation has been used but it demands on the computer resources. Therefore, it is only suitable for small structure less than about 100 atoms, discussed in Chapter 3. For $TiO_2$ nanowires calculation in Chapter 4, I have use GGA-PBE methods, keeping in mind that the findings are underestimated by 30-50%. Chapter 5 deals with a big system about 800 atoms, so SCC-DFTB is the best potential method for molecular dynamics simulation because of good structural description.

# CHAPTER III

# $n$-type doping of bulk anatase

*In this Chapter, I focus on Nb- and Ta-doped anatase $TiO_2$. The dopants Nb and Ta replace host Ti atoms, release their extra electrons, and transfer them to the host conduction band minimum. Heavily doped anatase behaves as a metal with high carrier concentration, and can be used for TCO applications, where the electrical conductivity is determined by the optical effective mass. The optical effective masses depend anisotropically on the carrier concentration, partly as a result of the nonparabolicity and partly because with increasing concentration higher branches of the CB become occupied. HSE06 which reproduces the width of the bands well gives the concentration dependence of the optical effective masses also in very good agreement with experiment. By calculating the formation energies, I have shown that Ta is a better dopant than Nb for TCO applications, because it is more soluble and has a smaller optical effective mass in the parallel direction. My calculations also explain the role of a reducing atmosphere in the efficient dopant incorporation.*

## 3.1 Structural properties

Anatase (body centered tetragonal) is one of crystalline modifications of $TiO_2$, the other two being rutile (tetragonal), and brookite (orthorhombic). The rutile is the most common natural form of $TiO_2$ while the metastable anatase phase converts

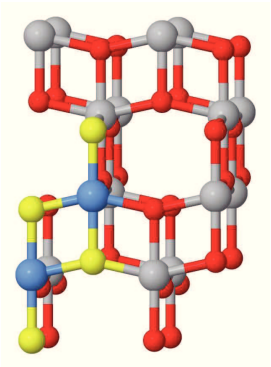

Figure 3.1: HSE06 48-atom supercell. Ti(blue) and O(yellow) are marked for the primitive cell while Ti(gray) and O(red) present other repeated cells.

| | HSE06 | Experiment |
|---|---|---|
| a (Å) | 3.755 | 3.782 |
| c (Å) | 9.561 | 9.502 |
| u | 0.207 | 0.208 |

Table 3.1: The HSE06 and experimental structural data of anatase.

to rutile upon heating. In this Chapter, I limit my investigations to anatase phase and its $n$-type doping for transparent conductor applications.

The anatase modification consists of two equivalent sublattices, with lattice constants $a, c$ orthogonal and parallel to the crystal axis, respectively. An internal parameter $u$ describes the relative position of the oxygen atoms. If a titanium atom of the first sublattice is located at the origin, its two apex oxygen atoms will be placed at $(0, 0, \pm uc)$. The first titanium neighbors are located at $(\pm a/2, 0, c/4)$ or $(0, \pm a/2, -c/4)$ and their two oxygen atoms are at $(\pm a/2, 0, c/4 \pm uc)$ or $(0, \pm a/2, -c/4 \pm uc)$, respectively (Figure 3.1).

As I mentioned in the previous Chapters, because of the success of hybrid functional HSE06 in describing the structural and electronic properties of $TiO_2$, I firstly use this approach to investigate the lattice parameters of anatase. The geometry of the perfect primitive cell has been optimized using a $8 \times 8 \times 8$ Monkhorst-Pack (MP set) [83]. Table 3.1 presents the lattice parameters of the anatase obtained by HSE06

| | $Ti_2O_4$ (B.C. tetra.) | $Ti_{16}O_{32}$ (tetra.) | $Ti_{32}O_{64}$ (tetra.) |
|---|---|---|---|
| $\vec{b_1}$ | $2\pi(0, \frac{1}{a}, \frac{1}{c})$ | $2\pi(\frac{1}{2a}, 0, 0)$ | $2\pi(\frac{1}{4a}, \frac{1}{4a}, 0)$ |
| $\vec{b_2}$ | $2\pi(\frac{1}{a}, 0, \frac{1}{c})$ | $2\pi(0, \frac{1}{2a}, 0)$ | $2\pi(\frac{1}{4a}, -\frac{1}{4a}, 0)$ |
| $\vec{b_3}$ | $2\pi(\frac{1}{a}, \frac{1}{a}, 0)$ | $2\pi(0, 0, \frac{1}{c})$ | $2\pi(0, 0, \frac{1}{c})$ |

Table 3.2: Reciprocal lattice vectors of unit cell and supercells of anatase.

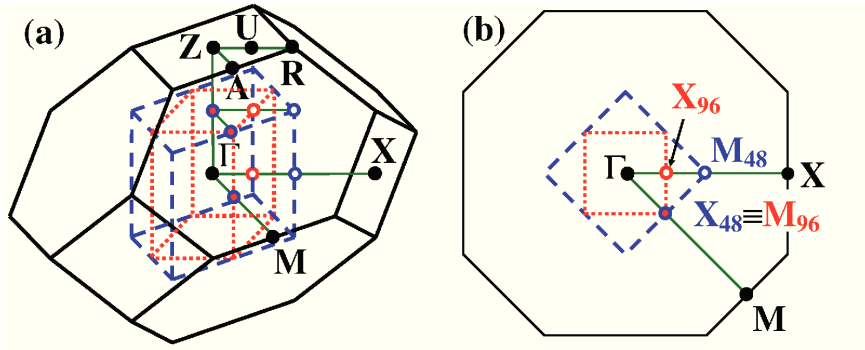


Figure 3.2: a) The BZ of the primitive (black line), the 48-atoms (blue dashed line) and 96-atoms (red dotted line) supercells. The letters refer to high symmetry points of the primitive BZ. b) The nesting of the BZs shown in the $k_z = 0$ plane.

and a comparison to experiment [84]. These HSE06 parameters are also used for all of my calculations in PBE for comparison.

## 3.2 Electronic properties

To calculate the electronic structure of doped anatase, I constructed many simple tetragonal supercells (from the body centered tetragonal primitive cell of 6 atoms) such as $1 \times 1 \times 1$ supercell (12 atoms), $\sqrt{2} \times \sqrt{2} \times 1$ supercell (24 atoms), $2 \times 2 \times 1$ supercell (48 atoms - Figure 3.1), $2\sqrt{2} \times 2\sqrt{2} \times 1$ supercell (96 atoms), and so on. A dopant is substituted for one Ti-atom of the supercell, therefore increasing the size of the supercell will decrease the dopant concentration. The Brillouin zones (BZs) of the primitive cell and the supercells are shown in Figure 3.2. The high symmetry points in $\frac{2\pi}{a}$ unit are listed in Table 3.3 where their positions are indicated in terms of the reciprocal lattice vectors defined in Table 3.2.

| coord. | $Ti_2O_4$ | $Ti_{16}O_{32}$ | $Ti_{32}O_{48}$ |
|---|---|---|---|
| $0,0,0)$ | $\Gamma$ | $\Gamma$ | $\Gamma$ |
| $(0,0,\frac{1}{2})$ | | Z | Z |
| $0,0,1)$ | Z | $2\Gamma$ | $2\Gamma$ |
| $(\frac{1}{4},0,0)$ | | X | M |
| $(\frac{3}{4},0,0)$ | M | 2X | 2M |
| $(\frac{1}{8},\frac{1}{8},0)$ | | | X |
| $(\frac{1}{4},\frac{1}{4},0)$ | | M | $2\Gamma$ |
| $(\frac{1}{2},\frac{1}{2},0)$ | X | $2\Gamma$ | $3\Gamma$ |
| $(\frac{1}{4},0,1)$ | A | X | M |
| $(\frac{1}{8},\frac{1}{8},1)$ | U | | X |
| $(\frac{1}{4},\frac{1}{4},1)$ | R | M | $2\Gamma$ |

Table 3.3: High symmetry points ($\frac{2\pi}{a}$ unit) in the BZ of primitive cell and supercells of anatase $TiO_2$

Figure 3.3 shows the band structure of the perfect lattice in the primitive BZ. By comparing the PBE and HSE06 results, I have found that the CB is considerably broader in the latter, which will lead to smaller effective masses, than those of Ref. [22]. Note that, in addition to the global minimum of the CB along the $M-\Gamma-X$ lines, there is a secondary minimum along the $A-Z-R$ lines. The secondary minimum is within 0.4 eV in energy from the global one in both calculations. In supercells, this minimum will fold back into the $\Gamma$ point of the reduced BZs and will appear as a low-lying higher branch of the CB.

I modeled doped anatase by 48- or 96-atom supercells with substituting a single titanium atom by Nb or Ta atom. This corresponds to dopand concentrations of 18.54 and $9.27\times10^{20}cm^{-3}$. PBE and HSE06 calculations for the self-consistent charge density $\rho(\mathbf{r})$ are applied with the special $k$-point sets for the BZ integration described in Table 3.4. Since the HSE06 total energy is changed less than 0.02 eV/primitive cell between the $8\times8\times8$ and the $4\times4\times4$ set for the primitive cell, and between the $4\times4\times2$ and the $2\times2\times2$ set for the 48-atom supercell, the charge densities of the smaller sets are used to calculate the $\varepsilon(\mathbf{k})$ dispersion relation at other $k$-points

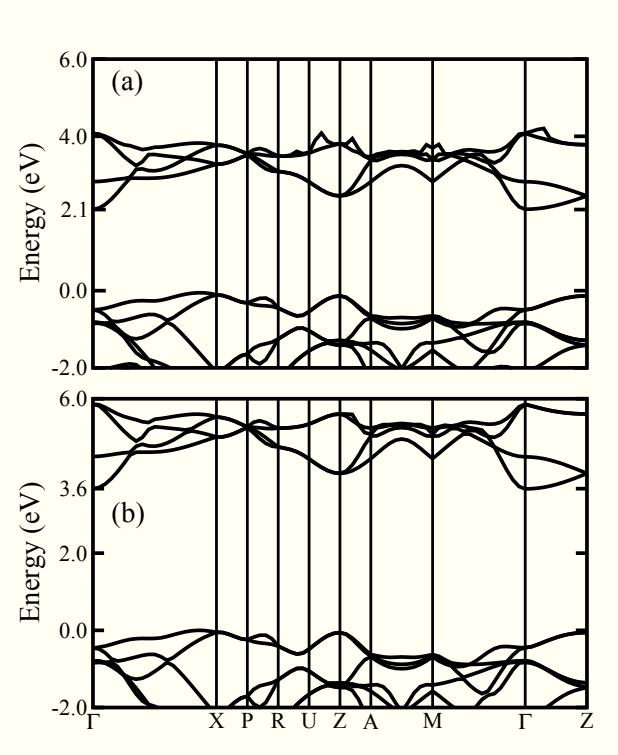


Figure 3.3: The PBE (a) and HSE06 (b) band structure of anatase in the primitive BZ. The valence band edges are taken as reference energy, and only the first four subbands are shown in each band.

for fitting. In case of the HSE06 functional, the required extra $k$-points have to be calculated self-consitently with zero weight. The energy of the defective supercells is minimized with respect to the atomic coordinates till forces are below 0.02 eV/Å.

I present the PBE conduction bands of 48- and 96-atom supercells with one dopant atom in each, corresponding to a fractions $x = 0.063$ and 0.031 of the cation sites in Figure 3.4. The CB of the perfect primitive cell ($x = 0.000$) is also shown. In the supercells, the dispersion relation folds back on the reduced BZ, but the degeneracy at the zone boundaries splits, because the introduction of the dopant reduces the symmetry from $D_{4h}$ to $D_{2d}$. Ta-doping seems to change only the band filling, it does not affect the band dispersion.

In HSE06 calculation, I only calculated the perfect cell and 48-atom supercell with one dopant atom. Figure 3.5 shows the corresponding conduction bands. From the HSE06 band structure of Nb-doping, the split between the first and second CBs at

| | | $1 \times 1 \times 1$ | $2\sqrt{2} \times 2\sqrt{2} \times 1$ | $2 \times 2 \times 1$ |
|---|---|---|---|---|
| $k$-set | PBE | $8 \times 8 \times 8$ | $2 \times 2 \times 2$ | $4 \times 4 \times 2$ |
| for $\rho(\mathbf{r})$ | HSE06 | $4 \times 4 \times 4$ | $2 \times 2 \times 2$ | |
| $k$-set | PBE | $16 \times 16 \times 16$ | $12 \times 12 \times 12$ | $24 \times 24 \times 12$ |
| for $\varepsilon(\mathbf{k})$ | HSE06 | $16 \times 16 \times 16$ | | $12 \times 12 \times 6$ |
| $N$ | | 6 | 96 | 48 |
| $x$ | | 0.000 | 0.031 | 0.063 |
| $n_{\mathrm{D}}$ | | 0.00 | $9.17 \times 10^{20}$ | $18.54 \times 10^{20}$ |

Table 3.4: The Monkhorst Pack sets in the PBE and HSE06 calculations for determination of the self-consistent charge density $\rho(\mathbf{r})$ and for $\varepsilon(\mathbf{k})$, as well as the total number of atom N, the Nb fraction $x$ per cation site, and the corresponding doping concentration $n_{\mathrm{D}}(\mathrm{cm}^{-3})$ are given.

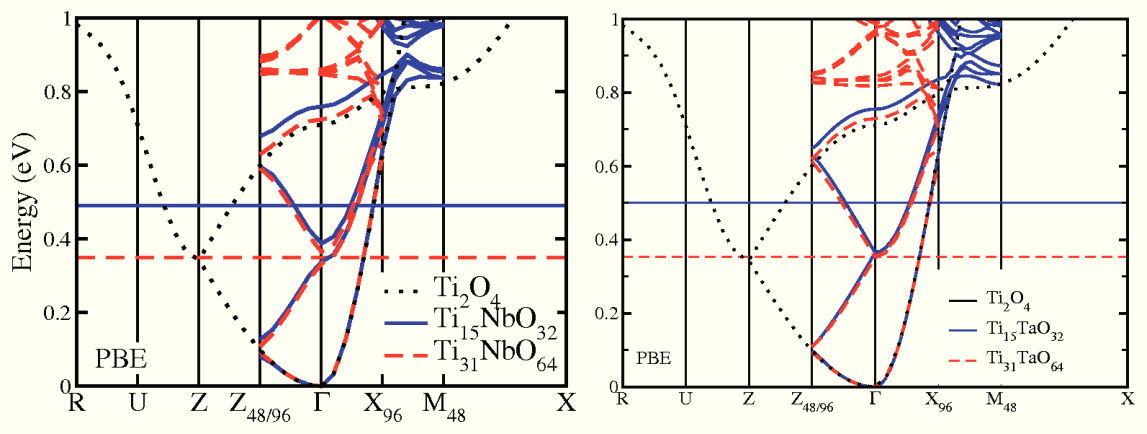


Figure 3.4: The PBE conduction band with Nb (left) and Ta (right) fraction of $x =$ 0.000 (black dotted line), 0.031 (red dashed line) and 0.063 (blue solid line), in the BZs of primitive, the 96-atom and the 48-atom supercell, respectively. Horizontal lines show the position of Fermi-energy.

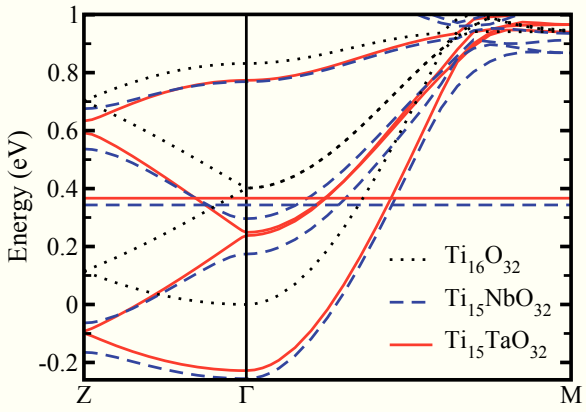


Figure 3.5: The HSE06 CBs with Ta/Nb fraction of $x = 0.063$ (red solid lines/blue dashed lines). The HSE06 CB of pure anatase is also represented by black dotted lines. Horizontal lines show the positions of Fermi-energy.

Z point is 0.10eV and 0.12eV for the second and third CBs at Γ point; while in case of Ta-doping, the small splits of the first two CBs and of the second-third CBs are 0.02eV and 0.01eV, respectively. Ta-dopant which has a $5d$ atomic orbital energy, higher than $4d$ one of Nb-dopant, does not change the Ti $3d$-nature conduction band. Both PBE and HSE06 band structures of doped anatase are aligned with perfect one. The alignment can be calculated by equilibrium shifting the average potentials of $TiO_2$ of perfect supercell and of $TiO_2$ which are unperturbed from the dopant. The result shows that, in HSE06, the CBMs of doped anatase shift down about 0.23-0.25eV with the perfect CBM.

The Fermi level at these concentrations is quite high above the CB edge, in agreement with the observed Burstein-Moss shifts in the onset of optical absorption [85]. In Nb-doping, for carrier concentrations of $n_e = 8\times10^{20}\text{cm}^{-3}$ and $n_e = 16\times10^{20}\text{cm}^{-3}$, it was observed that the Fermi level is above the CBM by 0.35 eV and 0.46 eV, respectively. Note that, the actual carrier concentration in the experiment was $\sim 83\%$ of the Nb concentration. My PBE(HSE06) values at $n_e = 9.27 \times 10^{20}\text{cm}^{-3}$ and $n_e = 18.54\times10^{20}\text{cm}^{-3}$, respectively, are 0.35(-) and 0.49(0.58)eV. Despite the virtual agreement of the PBE values with experiment, the HSE06 value is better, for the calculations with 17% higher concentrations.

From equation (2.38), to calculate the optical effective mass, we need to know the energy function $\varepsilon^{\ell}(\mathbf{k})$. This function can be found by fitting the band structure. Using a power expansion with $D_{2d}$ symmetry, I defined the energy function to fit points of the calculated conduction band as follow

$$\begin{aligned}\varepsilon^{\ell}(\mathbf{k}) = a_0^{\ell} + a_1^{\ell}(k_x^2 + k_y^2) + a_2^{\ell}k_z^2 + a_3^{\ell}(k_x^4 + k_y^4) + a_4^{\ell}k_z^4 + a_5^{\ell}k_x^2k_y^2 \\ +a_6^{\ell}(k_x^2k_z^2 + k_y^2k_z^2) + a_7^{\ell}|k_z| + a_8^{\ell}|k_z^3| + a_9^{\ell}(k_x^2 + k_y^2)|k_z|.\end{aligned} \tag{3.1}$$

The last three terms are needed for a good fit of higher bands, and the coefficients are an order of magnitude smaller than that of the first six (for $\ell = 1, a_{7,8,9}^1 = 0$). The fitting is performed to an energy higher than the actual Fermi energy but lower than the minimum of the bands $\ell > 3$. The mean square error of resulting fits in all cases are lower than 0.01eV.

## 3.3 Optical effective mass

### 3.3.1 Optical effective mass of Nb-doped anatase

To calculate the optical effective mass, I have two assumptions. First, the carrier concentration equals the dopant concentration, $n_e = n_{\mathrm{D}}$. Hence, I can determine the Fermi level at any dopant fraction. In the vicinity of a given dopant concentration, the band structure does not change too much. Therefore, I can extrapolate the value of the optical effective mass as a function of the carrier concentration at least within a narrow range by carrying filled for a given concentration.

By calculating from equation (2.38), I show the values of the optical effective mass as circles in Figures. 3.6. At small concentration, the difference is small between the PBE and HSE06, but the latter become gradually lower with increasing concentration. This is due to the wider bands in HSE06 with respect to PBE. Then, I determined the

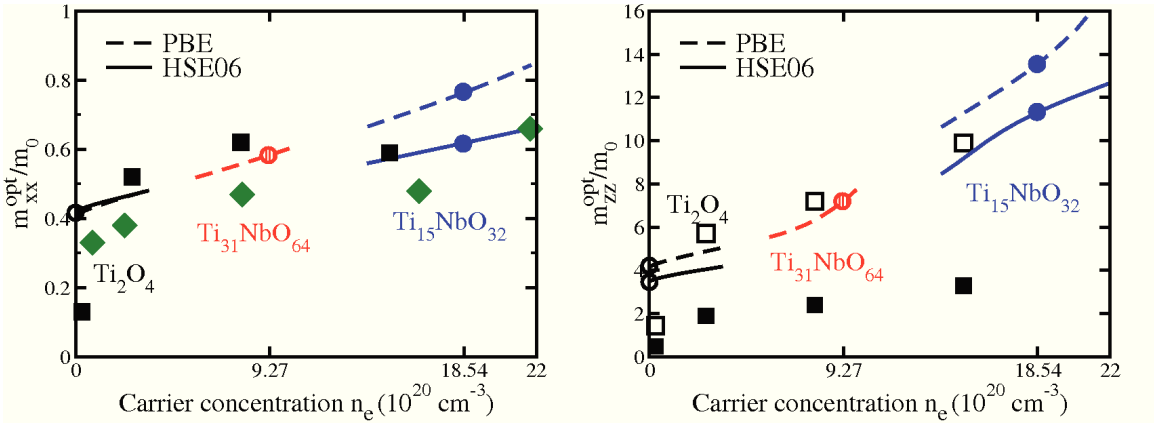


Figure 3.6: The carrier concentration dependence of the optical effective mass in the orthogonal (left) and parallel (right) directions to the main axis. Full, hatched, and empty circles denote the values calculated from the band structures of the 48- and 96-atom supercells (with one Nb atom each) and from the perfect primitive cell, respectively. Lines are extrapolations based on the PBE (dashed lines) and HSE06 (solid lines) band structures. Experimental data are represented by diamonds (Ref. [27]) and squares (Ref. [28]) The empty squares are the multiplied experimental values [28] by the factor $[(m_{\parallel} - m_{\perp})/m_{\perp}]^{1/2}$.

contribution of the optical effective mass of each bands in Figure. 3.7. From this figure, in the concentration range relevant for the TCO application, I have found that the increase of $m^{\text{opt}}$ is strongly influenced by the contributions of the 2$^{\text{nd}}$ and 3$^{\text{rd}}$ bands, not just by the non-parabolicity of the 1$^{\text{st}}$ one. The lower values of the former in the HSE06 case keep the orthogonal effective masses within range of the experimental data, while the PBE values give an increase of overestimation (Figure 3.7).

The dashed and the solid lines around the last data points in Figure 3.6 represent the optical effective masses in the parallel direction. PBE predicts a concave curve while HSE06 a convex one for high concentrations, respectively. Multiplying the experimental results [28] with a factor of $[(m_{\parallel} - m_{\perp})/m_{\perp}]^{1/2}$ gives an excelent agreement with the calculated masses (except for the lowest concentration, where the metallic conduction is lost [16].

The optical effective mass in the parallel direction is much higher than that of

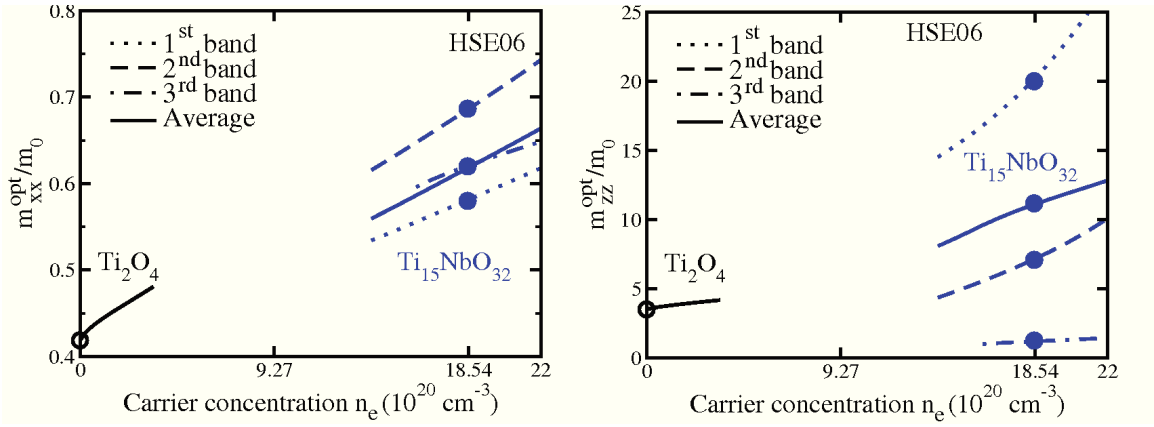


Figure 3.7: Dotted, dashed, and dot-dashed lines are the contributions of the average optical effective mass for the first, second, and third HSE06 sub-bands, respectively in the direction orthogonal (left) and parallel (right) to the main axis.

the orthogonal one, and for large carrier concentration the anisotropy increases even further. This is mainly due to the steepness increased in the contribution of the first band (in Figure 3.7, ). I have found, however that $\varepsilon(\mathbf{k})$ becomes extremely flat along the lines parallel to $\Gamma - Z$ in the $\Gamma - Z - R - X$ plane (Figure 3.8). Note that the contribution of the third band diminishes the anisotropy due to the more symmetric nature of the secondary minimum in the CB.

### 3.3.2 Comparison of optical effective mass between Nb- and Ta-doped anatase

In the previous section on Nb-doped anatase, I used the volume integral, the second derivative of the $|k_z|$ term did not contribute to the optical effective mass. Therefore, the values for parallel mass may be less exact. This is even more so in the case of Ta. When the dispersion relation has a significant contribution from the term which have a discontinuous derivative. The Gauss theorem cannot be applied, equation (2.37) cannot be rewritten into a volume integral of the second derivative (2.38). In this section, I have calculated the surface integral using finite differences

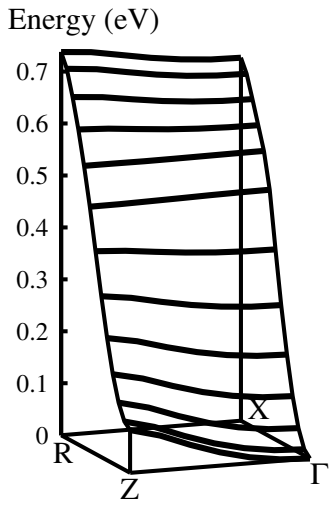


Figure 3.8: The PBE $\varepsilon(\mathbf{k})$ relation in the $\Gamma - Z - R - X$ plane of the BZ corresponding to the 48-atom supercell.

in the perfect anatase unit cell and for both Nb- and Ta-doped cases. Details of calculation is shown in Appendix A.

Figure 3.9 shows the comparison of the optical effective masses in orthogonal and parallel directions to the main axis of Nb- and Ta-doped anatase by using surface integral. Calculating the orthogonal optical effective masses in a range of carrier concentration from 0 up to $2.2\times10^{21}\text{cm}^{-3}$, I got both Nb-doped and Ta-doped anatase TiO2, from $0.41m_0$ to $0.8m_0$ in PBE, and between $0.4m_0$ and $0.6m_0$ in HSE. In the parallel direction, the optical effective mass of the Nb-doping changes from $4.1m_0$ to $14.6m_0$ in PBE and from $3.5m_0$ to $12.4m_0$ in HSE06, slightly lower than our previous volume integral calculation. Testing without the contribution of $|k_z|$ term, I found that the values of parallel optical effective mass of Nb-doped anatase (using surface integral) absolutely fit with the previous calculated results (using volume integral). The linear $|k_z|$ part becomes significant to reduce the parallel optical effective mass.

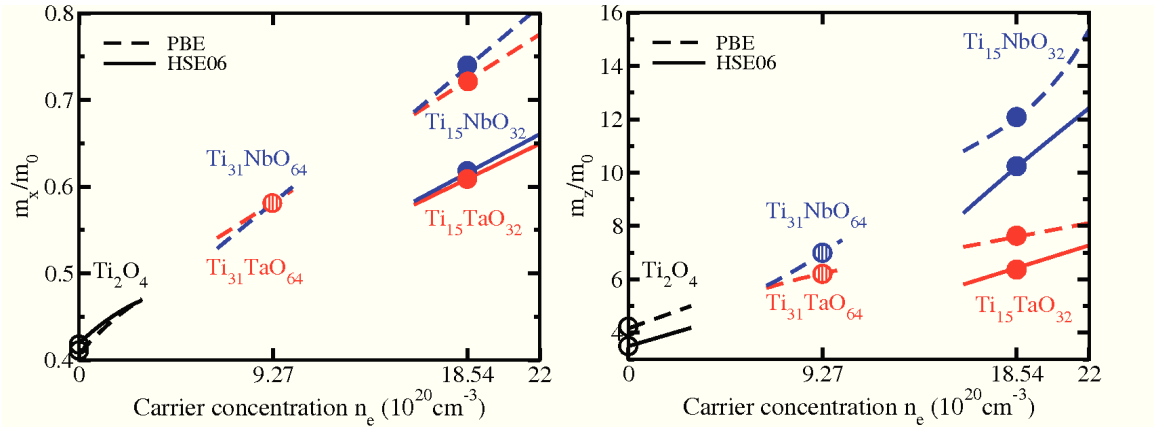


Figure 3.9: The carrier concentration dependence of the orthogonal effective mass of Ta- (red) and Nb-doping (blue) in PBE (dashed lines) and HSE (solid lines) calculation. Full, hatched and empty spheres and squares denote the values calculated from the band structures of 48- and 96-atom supercells (with one Ta/Nb atom each), and from the perfect primitive cell, respectively. Lines are extrapolations based on band structures.

The parallel optical effective mass of Ta-doping changes linearly from $4.1m_0$ to $8.1m_0$ in PBE and $3.5m_0$ and $7.3m_0$ in HSE06 as the carrier increases. A small split between conduction bands in Ta-doping makes a smaller parallel optical effective mass. Ta-dopant has a better optical effective mass than Nb-one does in anatase.

## 3.4 Formation energies of substitutional Nb and Ta

To replace a host atom by a dopant, we need an energy to break atomic bonds and stress lattice. In doped anatase, the formation energy of the defect D (D=$Nb_{Ti}$,$Ta_{Ti}$) is calculated as a function of the chemical potentials of bulk $TiO_2$, Ti, and D by the expression [86]

$$E_{\mathrm{f}} = E_{\mathrm{tot}}(\mathrm{Ti}_{n-1}, \mathrm{O}_{2n} : \mathrm{D}) - n\mu^{\mathrm{bulk}}_{\mathrm{TiO_2}} - (\mu_{\mathrm{D}} - \mu_{\mathrm{Ti}}), \tag{3.2}$$

where $E_{\text{tot}}$ is the total energy of the supercell with one dopant each, $n$= 16 or 32 is the number of units in the supercells, $\mu^{\text{bulk}}_{\text{TiO}_2}$ is the energy of one unit in the perfect crystal

The chemical potential $\mu_{\text{Ti}}$ and $\mu_{\text{D}}$ depend on the experimental growth conditions, which can be O-poor, O-rich or any thing in between. The former is connected to the chemical potential of oxygen by the equilibrium condition

$$\mu_{\text{Ti}} + 2\mu_0 = \mu^{\text{bulk}}_{\text{TiO}_2}. \tag{3.3}$$

The limiting values occur in the extreme O-rich case which places a limit on $\mu_O$ given by $\mu_O = \frac{1}{2}\text{O}_2(\text{p,T})$ and in the extreme O-poor case, when $\text{Ti}_2\text{O}_3$ is formed instead of $\text{TiO}_2$, equation (3.3) becomes

$$2\mu_{\text{Ti}} + 3\mu_0 = \mu^{\text{bulk}}_{\text{Ti}_2\text{O}_3}. \tag{3.4}$$

The total energy of $\text{TiO}_2$ and $\text{Ti}_2\text{O}_3$ can also be expressed as

$$\begin{cases} \mu^{\text{bulk}}_{\text{TiO}_2} = \mu^{\text{bulk}}_{\text{Ti}} + \mu_{\text{O}_2(\text{p,T})} + \Delta H_{\text{f}}^{\text{TiO}_2}, \\ \mu^{\text{bulk}}_{\text{Ti}_2\text{O}_3} = 2\mu^{\text{bulk}}_{\text{Ti}} + \frac{3}{2}\mu_{\text{O}_2(\text{p,T})} + \Delta H_{\text{f}}^{\text{Ti}_2\text{O}_3}, \end{cases} \tag{3.5}$$

where $\Delta H_{\text{f}}^{\text{TiO}_2}$ and $\Delta H_{\text{f}}^{\text{Ti}_2\text{O}_3}$ are the enthalpies of formation.

For dopant, similarly, we need to consider the chemical potential of dopant $\mu_{\text{D}}$ equilibrium with its dopant oxide by

$$2\mu_{\text{D}} + 5\mu_0 = \mu^{\text{bulk}}_{\text{D}_2\text{O}_5} = 2\mu^{\text{bulk}}_{\text{D}} + \frac{5}{2}\mu_{\text{O}_2(\text{p,T})} + \Delta H_{\text{f}}^{\text{D}_2\text{O}_5}. \tag{3.6}$$

The enthalpy of dopant oxides $\text{Nb}_2\text{O}_5$ and $\text{Ta}_2\text{O}_5$ can be calculated by PBE and HSE06. However, at low temperature, the crystalline bulk phases of both dopant oxides are not uniquely determined. For $\text{Nb}_2\text{O}_5$, many configurations have

Table 3.5: Formation energy $E_{\mathrm{f}}$ (eV) of Nb and Ta-doped anatase $TiO_2$

| $V_{\mathrm{xc}}$ | Structure | O-rich | Stoichiometric | Ti-rich |
|---|---|---|---|---|
| PBE | $Ti_{31}NbO_{64}$ | 2.46 | 1.25 | 0.62 |
| | $Ti_{31}TaO_{64}$ | 2.01 | 0.80 | 0.16 |
| | $Ti_{15}NbO_{32}$ | 2.71 | 1.50 | 0.87 |
| | $Ti_{15}TaO_{32}$ | 2.28 | 1.06 | 0.43 |
| HSE | $Ti_{15}NbO_{32}$ | 2.42 | 1.20 | 0.57 |
| | $Ti_{15}TaO_{32}$ | 1.90 | 0.68 | 0.05 |

been observed including P-$Nb_2O_5$ (low heating), N-$Nb_2O_5$ (rapid heating), R-$Nb_2O_5$ (metastable), M-$Nb_2O_5$ (medium temperature), H-$Nb_2O_5$ (high temperature), T-$Nb_2O_5$, B-$Nb_2O_5$ (high-pressure phases) while $Nb_2O_5$ is amorphous at low temperature.[87, 88] For $Ta_2O_5$, at least the phases of $\beta$-$Ta_2O_5$ (orthorhombic), $\delta$-$Ta_2O_5$ (hexagonal) have been found. [87, 89, 90, 91] Therefore, instead of being theoretically calculated, the values of enthalpy $\Delta H_{\mathrm{f}}$ are taken by the previous experiment of -19.687eV for $Nb_2O_5$ and of -21.205eV for $Ta_2O_5$. [92]. Note that the enthalpy values of both $TiO_2$ and $Ti_2O_3$ are also taken from experiment.

Table 3.5 shows the formation energy of Nb- and Ta-doped anatase $TiO_2$ in PBE and HSE calculations. At a given dopant concentration, the formation energy obtained from the HSE calculation is smaller than the energy obtained from PBE calculation. Moreover, for either the PBE or HSE functionals, the formation energy of the Ta-doping is smaller than that of Nb-doping. Ta-dopant is more soluble than Nb-one.

The formation energy in the O-poor condition smaller than in O-rich of $\Delta H_{\mathrm{f}}^{\mathrm{TiO_2}} - \frac{1}{2}\Delta H_{\mathrm{f}}^{\mathrm{Ti_2O_2}}$. Therefore, the reducing atmosphere during growth [33, 22, 31] is necessary because the formation of Ta- and Nb-oxides is more exothermic than that of $TiO_2$. In the observation of the Kamisaka *et al.* [23], there is the heater of formation of Nb-$V_O$ in anatase. The authors assumed that oxygen vacancies are important, so they concentrated their studies on Nb-$V_O$ interactions. In fact, vacancies are not necessary

for the conductivity, the reducing treatment only improves the dopant incorporation to Ti sites.

From the comparison between Nb- and Ta-doped anatase, I found that Ta has the considerably higher solubility and lower optical effective mass of the two dopants. Therefore, Ta is a better dopant than Nb for TCO applications. Although Ta may differently affect the crystallization procedure, further experiment with it can be recommended.

# CHAPTER IV

# $TiO_2$ nanowires and their doping by Nb and Ta

*This chapter discusses about anatase nanowires and their doping by Nb and Ta. First, I review the structural and electronic properties of perfect anatase nanowires. It is shown that the symmetry plays an important role in the stability and characteristics of the band structure. In the second part, I investigate the most favoured substitutional dopant positions and the influence of the high symmetry upon the conduction band of nanowires.*

## 4.1 Anatase $TiO_2$ nanowires

### 4.1.1 Structural and stability properties

The crystal structure determines the electronic and optical properties of the nanowires (NWs). Understanding how and why NWs take the form they do is an important key to develop many nano devices. In this part, I have concentrated on the model proposed by Liu and Yang [37] for the structure of their experimentally observed anatase nanowire (ANW) with diameters of 5 Å. Such [001] ANWs were synthesized by using a nonhydrolytic solution approach. The HRTEM images of such a wire are shown in Figure 4.1.

Theoretically, models of NWs are generally constructed by cutting the 3D crystal

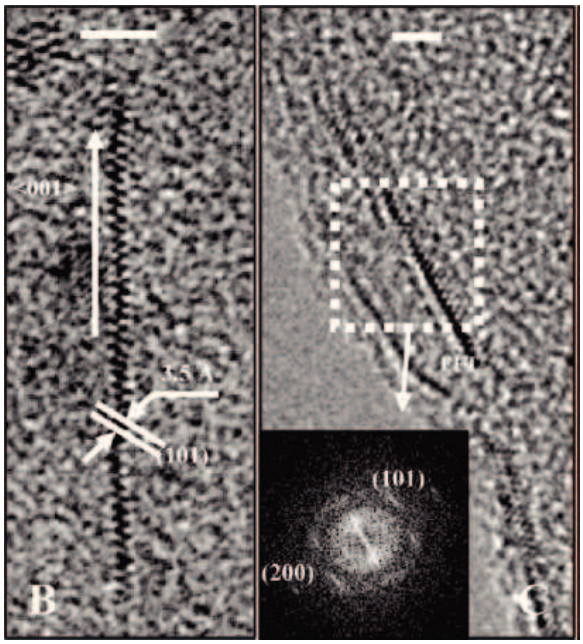


Figure 4.1: (B) HRTEM image of a [001] ANW with a diameter of around 4.3 Å and lattice fringes spaced at about 3.5 Å intervals, corresponding to the spacing between the (101) planes of anatase $TiO_2$. (C) HRTEM image of ANWs with the corresponding FFT pattern in the inset. Reproduced from Ref.[37]

along axis of the NWs. As we know, the symmetry of the bulk anatase crystal can be decribed by a body-centered tetragonal lattice with a space group symmetry $D_{4h}^{19}$-$I4_1/amd$. [93] This nonsymmorphic space group contains 4-fold screw axes parallel to the $z$ axis going through the interstitial regions of the crystal with atoms at the corners and edges of the concentric squares around the axes. [3] A rotation by $\pi/4$ around the axes followed by a shift of $c/4$ along the $z$ axis maps the crystal onto itself (where $c$ is the lattice constant of the Bravais cell in the $z$ direction). Figure 4.2 shows these screw axes and other 2-fold rotation axes going through crystal atoms without screw symmetry.

Recently, Iacomino *et al.* have proposed the model of [001] ANWs with {100} side walls centered around the 2-fold rotation axis.[39]. These NWs have a symmorphic line group with the point group $D_{2d}$ and lose the screw symmetry of the bulk crystal. However, by cutting such wires around the screw axis of the bulk crystal, Aradi *et al.*

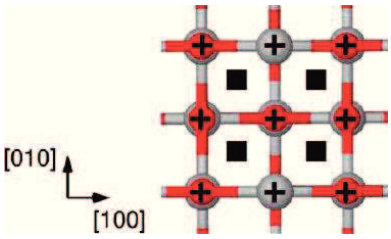


Figure 4.2: View of the anatase bulk crystal from the [001] direction. The squares mark the 4-fold screw axes while the crosses mark the simple 2-fold rotation axes. The titanium and oxygen atoms are represented by big gray and small red spheres, respectively.

involved a new model of stoichometric [001] ANWs with point group $D_4$. [3] These NWs retain the nonsymmorphic character of the bulk space group and have a 4-fold rotation in their point group. The relaxed geometries without and with screw axis are shown in Figure 4.3 and Figure 4.4. The numbers in the name of each NW indicate the numbers of $TiO_2$ units ($n$$TiO_2$) in the elementary cell of the NW. The NWs A9, A25, and A49 are identical to those studied by Iacomino *et al.* while the NWs A16, A36, and A64 are built by Aradi *et al.* The smallest nanowire with screw axis A4 spontaneously relaxes to a chain-like structure identical to the one investigated by Zhang *et al.*[38]

The thinnest nanowires A4 and A9 do not keep the original anatase structure. The starting A4 structure of $D_4$ symmetry does not contain fully coordinated Ti atoms at all, all titanium atoms coordinate to four oxygen atoms while all oxygen atoms coordinate to two titanium atoms. The starting A9 structure of $D_{2d}$ symmetry has one 4-fold Ti atom per unit cell.

The formation energy of the NWs can be defined as

$$E_{\mathrm{f}}^{\mathrm{NWs}} = \frac{E_{\mathrm{tot}}^{\mathrm{NWs}} - n_{\mathrm{TiO_2}} E_{\mathrm{TiO_2}}^{\mathrm{bulk}}}{n_{\mathrm{TiO_2}}} \tag{4.1}$$

with $n_{\mathrm{TiO_2}}$ being the number of $TiO_2$ units in the NW.

The formation energies of ANWs are shown in Figure 4.5. {100}-walled NWs

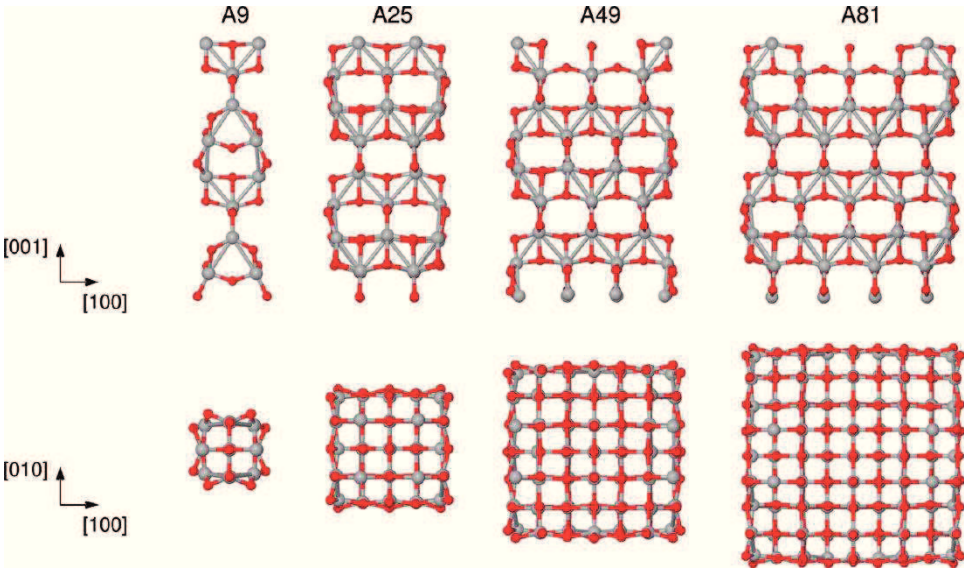


Figure 4.3: Side and top view of the relaxed [001] ANWs without screw axis built by Iacomino *et al.* The side views show two unit cells. Big gray and small red circles indicate the titanium and oxygen atoms, respectively.

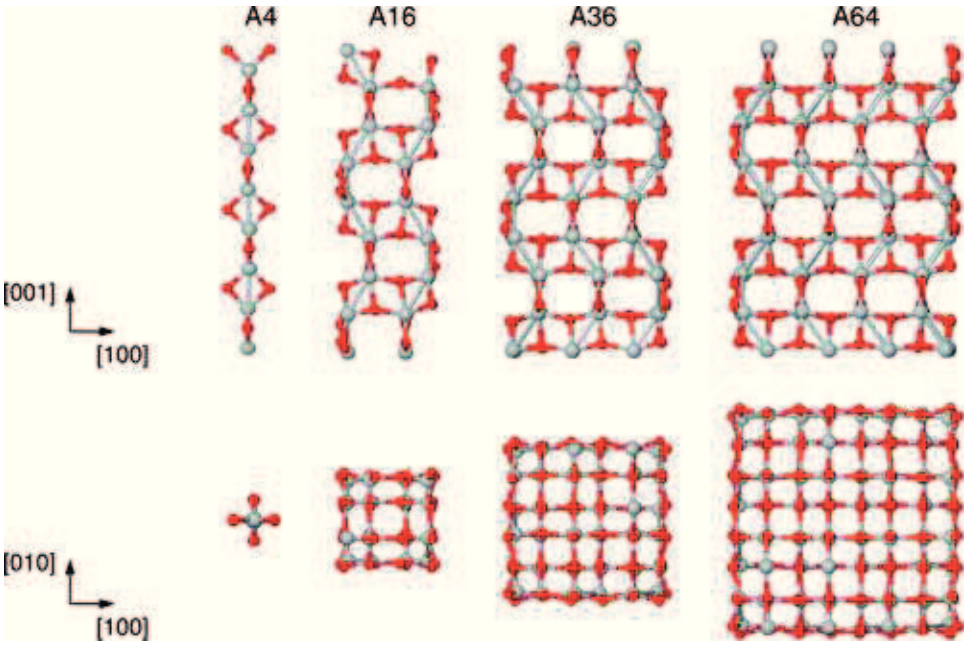


Figure 4.4: Side and top view of relaxed [001] ANWs with screw axis built by Aradi *et al.*. The side views two unit cells. Big gray and small red cicles indicate the titanium and oxygen atoms, respectively. The thinest wire A4 with screw axis spontaneously relaxes to a chain-like structure identical to the one investigated by Zhang *et al.*

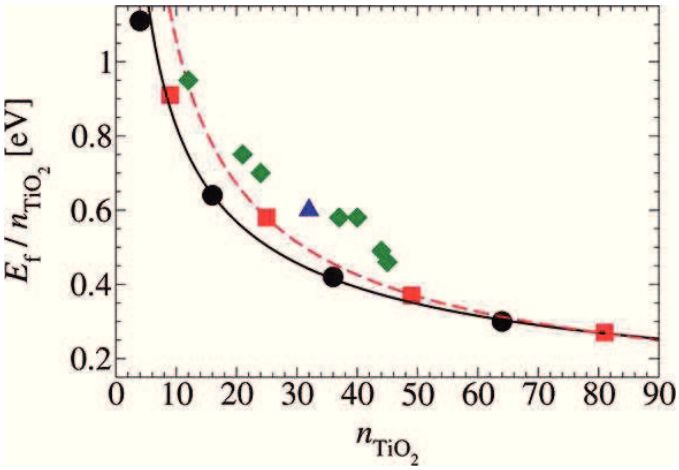


Figure 4.5: Formation energy per $TiO_2$ unit for bare stoichiometric [001] anatase wires. Black circles and red squares stand for {100}-walled anatase wires with screw symmetry (point group $D_4$) and plain rotation symmetry (point group $D_{2d}$), respectively. Blue triangle marks the anatase wire with reconstructed {100} side walls. Wires with other side walls than {100} are indicated by green diamonds (see detail in Ref. [3]).

without and with screw axis in are compared to ones with other side walls. It can be seen that {100}-faceted wires are more stable than others, and the NWs keeping the nonsymmorphic characteristics (the screw axis) of the parent crystal are the most stable. The thinnest NWs which keep the anatase structure are A9 and A16 without and with screw axis. Simulated HRTEM images clearly show that the nanowire without the screw axis (A9) gives rise to an apparent mirror symmetry, while the nanowire with the screw axis (A16) produces an image which resembles a zigzag line (in Figure 4.6). Clearly, the published previous HRTEM images of Liu and Yang [37] (Figure 4.1) show a zigzag-like structure without mirror symmetry. This proves that the more stable screw-symmetric (A16) structure had, in fact, been observed in the experiment and not the mirror symmetric (A9) one. [1]

[1]This section is in joint authorship with B. Aradi

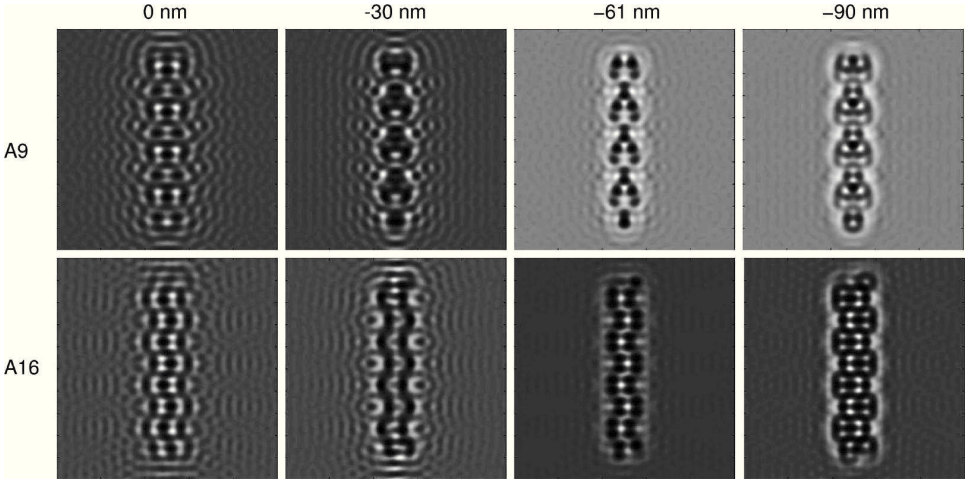


Figure 4.6: Simulated HRTEM images based on the relaxed anatase nanowires A9 and A16. Values above the columns indicate the defocus length with 61 nm corresponding to the Scherzer optimum defocus length. In the pictures with defocus lengths of 61 and 90 nm the Ti (O) atoms are black (white) and white (black), respectively. Reproduced from Ref.[3]

### 4.1.2 Electronic properties

Bulk anatase has an indirect band gap with the CBM at the Γ point and the VBM along the ΓX line (near X point). However, the [001] ANWs have a direct gap at Γ. The band gaps of the nanowires with screw symmetry (A4, A16, A36, A64) were predicted higher than without it (A9, A25, A49, A81). [3] Figure 4.7 shows the band line-up of the ANWs with screw symmetry (A4, A16, A36, A64 columns). The bands were aligned based on the average electrostatic potential across the cross section. The band gap decreases with an increasing diameter, as one would expect, due to the decreasing quantum confinement. Anatase bulk is also included for comparison ($TiO_2$ column). Due to a practical limitation, I carried out these calculations with the PBE functional only, keeping in mind that the band gaps are underestimated by $30 - 50\%$.

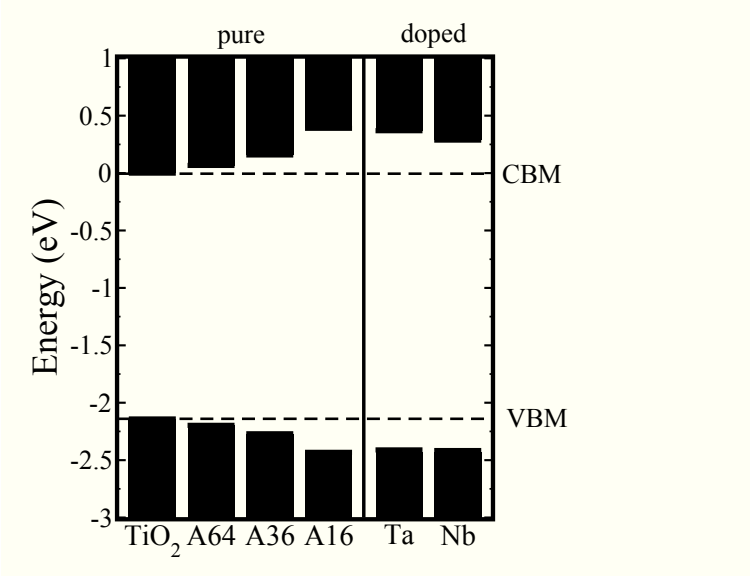


Figure 4.7: Band line-up of the pure ANWs (left) and doped-A16 with one dopant Nb or Ta at sub-corner Ti site in one unit cell (right). Band structure of perfect anatase bulk ($TiO_2$ column) are included for comparison and dashed horizontal lines show its HOMO and LUMO.

## 4.2 Nb- and Ta-doped anatase nanowires

### 4.2.1 Structural properties

Nb- and Ta-dopant can replace the Ti host atom in anatase nanowires and release extra electrons to the host conduction band. The most stable pure ANWs were chosen for doping. The question arises which position is preferred for dopant substitution. In order to investigate this, I have calculated the formation energies in various positions. Formation energy is calculated from equation (3.2), divided by the number of dopants in one cell. Figure 4.8 shows the available sites in A16 and A36 (with screw axis). The dopant can be placed at the corner of the ANW (having 4 oxygen neighbours, noted by $^{(1)}$), at sub-corner or inner site (having 6 oxygen neighbours, noted by $^{(3)}$,$^{(6)}$, respectively) and at the surface or sub-surface site (having 5 oxygen neighbours, noted by $^{(2)}$,$^{(4)}$ ,$^{(5)}$, respectively).

Table 4.1 shows the formation energies of the doped A16 and A36 nanowires. The formation energy strongly depends on the position of the dopant. I have found that

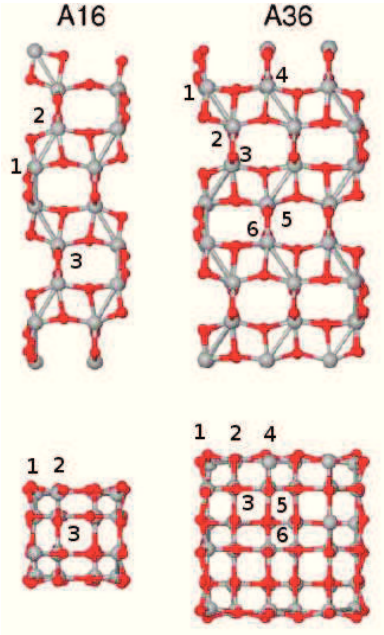


Figure 4.8: Side and top view of available positions of dopant in A16 and A36 nanowires. Dopant can be placed at the corner [(1)], surface [(2),(4)], sub-corner [(3)], sub-surface [(5)], and inner [(6)] Ti sites.

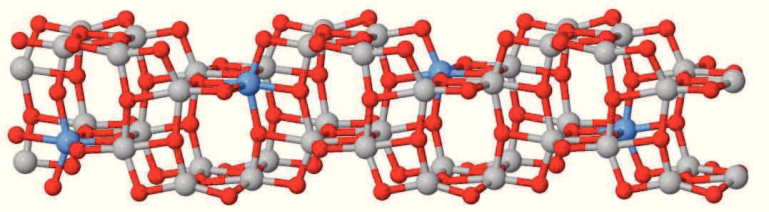

Figure 4.9: Structure of $A16_3$-$Ta_4$ nanowire with the highest symmetry of $D_4$. Big gray, blue, and small red cicles indicate the titanium, tantalum and oxygen atoms, respectively. Four tantalum atoms substitute four host full-coordinated titanium atoms (sub-corner [(3,3,3,3)]) in three unit cells of wire.

the most favoured site is the sub-corner position while the corner site is the least attractive for the dopant. The corner site has 4 oxygen atoms only, so replacement of nominally tetravalent Ti with pentavalent Ta is energetically costly. In contrast, a titanium at sub-corner site is fully coordinated, and a substitutional Ta will act as a donor at little energy cost. The formation energy of Ta inner sites is also high because of the reduced relaxational freedom. Comparing the thicker nanowire (A36) with the thinner one (A16), solubility increases with thickness, as expected. Assuming that Nb-dopant has the same behavior as Ta in ANWs, I have also considered Nb-doping at the most preferable position, the results show that Ta is more soluble than Nb, which is similar to the bulk doping in anatase.

### 4.2.2 Band structure

Figure 4.7 shows the band line-up of Nb- and Ta-doped A16. The alignment was determined by means of the average potential of atoms on cross section far away the dopant. Similar to doping in bulk anatase, the dopant in the ANW introduces shallow effective mass-like states, i.e. a shift in the CB edge. For example, I have compared the conduction bands of Nb- and Ta-doped A16 nanowires (Figure 4.10a). In case of Ta-doping, Ta substitutes at sub-corner site. The CB is similar to the CB of the perfect ANW, with small splitting between the first two CB branches. In contrast, Nb gives a big splitting between the first and second branches. As can be seen, Nb is also a deeper donor than Ta in the ANW.

To investigate the role of high symmetry in the doped-ANWs, I have doubled the dopant concentration and investigated different arrangements of the two dopants in the same cell. In the most favoured arrangement, both dopants are at sub-corner sites (noted by $^{(33)}$) having the $D_2$ symmetry. The conduction bands of this arrangement is shown in Figure 4.10c. There is no splitting between the first two conduction branches. This effect is similar to bigger wires A36. Testing with two dopants at

| Structure | Dopant position | $E_f/n_D$ | Symmetry |
|---|---|---|---|
| A16-$Ta_1$ | (1) | 1.65 | $C_1$ |
| | (2) | 1.17 | $C_1$ |
| | (3) | **0.95** | $C_1$ |
| $A16_3Ta_4$ | (3333) | **0.96** | $D_4$ |
| A16-$Ta_2$ | (11) | 1.69 | $D_2$ |
| | (33) | **1.00** | $D_2$ |
| A36-$Ta_1$ | (1) | 1.27 | $C_1$ |
| | (2) | 0.84 | $C_1$ |
| | (3) | **0.53** | $C_1$ |
| | (4) | 0.87 | $C_1$ |
| | (5) | 0.65 | $C_1$ |
| | (6) | 0.80 | $C_1$ |
| A36-$Ta_2$ | (11) | 1.29 | $D_2$ |
| | (33) | **0.55** | $D_2$ |
| | (35) | 0.63 | $C_1$ |
| | (55) | 0.69 | $C_2$ |
| | (66) | 0.90 | $C_2$ |
| A16-$Nb_1$ | (3) | **1.88** | $C_1$ |
| $A16_3Nb_4$ | (3333) | **1.86** | $D_4$ |
| A16-$Nb_2$ | (33) | **1.90** | $D_2$ |
| A36-$Nb_1$ | (3) | **1.50** | $C_1$ |
| A36-$Nb_2$ | (33) | **1.51** | $D_2$ |

Table 4.1: Formation energy (in eV/number of dopant) and symmetry of Nb-,Ta-doped anatase wires. Number (i),(ij),or (iiii) indicate the position of 1, 2 or 4 dopants in ANWs, respectively (see Figure 4.8).

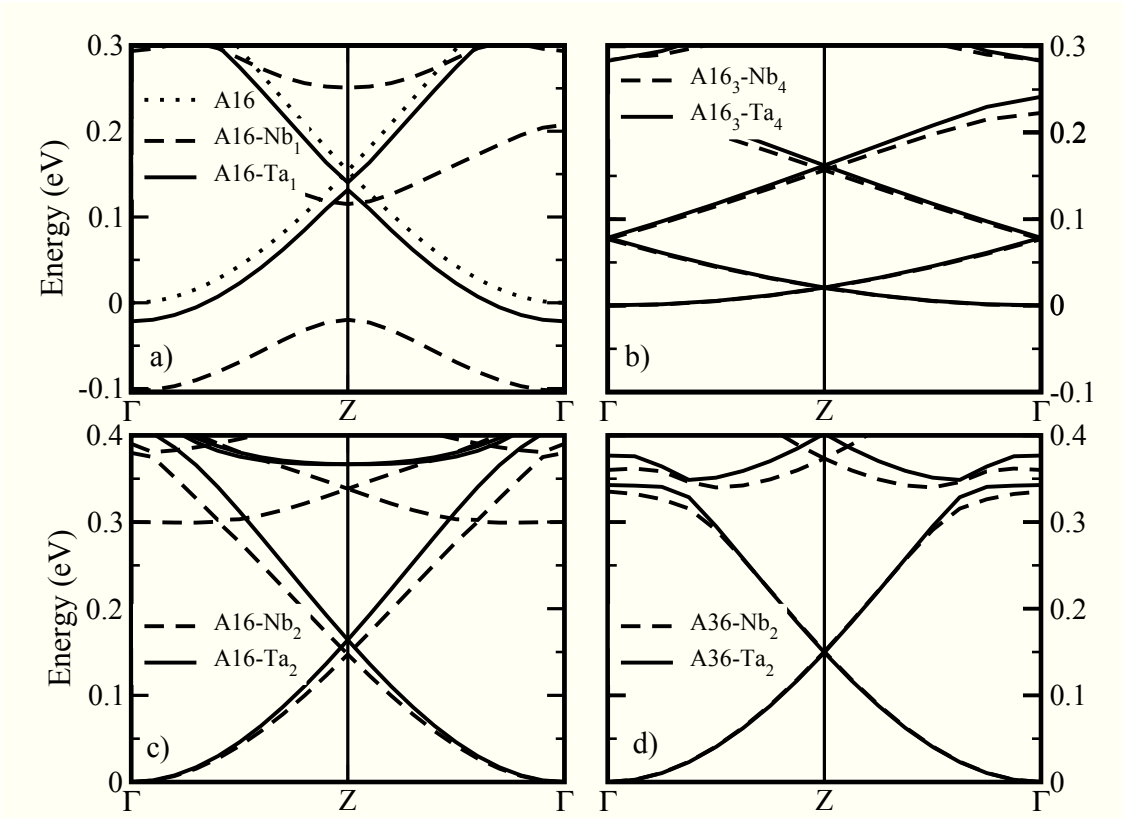


Figure 4.10: The conduction band of doped ANWs. Dopants place at sub-corner Ti sites. a) One dopant atom replaces Ti atom in one unit cell of A16. b) Four dopant atoms replace four Ti atoms in three unit cell of A16. c) Two dopants replace two Ti atoms in one unit cell of A16. d) Two dopants replace two Ti atoms in one unit cell of A36. The dot, dashed, and solid lines are the CBs of pure, Nb-doped, Ta-doped ANWs, respectively. The CBs in a) are aligned by average potential calculation (comparing with Figure 4.7) while the CBMs in the rest ones b), c), d) are set to zero.

sub-corner sites in the bigger wire A36 (also symmetry $D_2$ ), I have also got the same effect (Figure 4.10d).

Doping 4 dopant atoms to 3 unit cells of A16 nanowires, I have found that the doped nanowires have the highest symmetry of $D_4$, dopants replace Ti atoms at the sub-corner sites (Figure 4.9). The doped nanowires contain 4-fold screw axis parallel to the $z$ axis. A rotation by $\pi/4$ around the axis combining a shift of $3c/4$ along the $z$ axis maps the nanowire onto itself. The CBs of Nb- and Ta-doped A16 wires are shown in Figure 4.10b. The dispersion relation folds back onto the reduced BZ and the degeneracy at the zone boundary does not split because the screw axis is

restored. Therefore, even in doped ANW, the stability is strongly influenced by the presence of the screw axis. The likely reason is that keeping the symmetry uninvites the perturbation of the electronic structure.

# CHAPTER V

# Rutile/Anatase heterojunction

*Mixing anatase and rutile powders gives a higher photocatalytic activity than that of the pristine phases. This increase is generally attributed to charge separation between the phases, due to a staggered band line-up. Here, a theory of the band alignment across the rutile(100)/anatase(100) interface is presented and I conclude that electrons are transfered from rutile to anatase, while holes move in the opposite direction.*

## 5.1 Building the interface

The most stable rutile surface is a (110) surface while the most stable anatase one is a (101) surface. Computational studies indicated a surface stability order of (110) > (100) > (011) > (001) for rutile [94, 93], and of (101) > (100) > (001) for anatase [95]. Therefore, many interfaces can be formed between $TiO_2$ grains. I have utilized a slab model for the interface between rutile and anatase. Since I used a plane wave basis (in VASP), the model had to be 3D periodic, containing - besides the rutile and the anatase layer, also a vacuum layer of appropriate thickness to decouple the repeated slabs. The vacuum size and the thickness of each slab should be big enough that the interactions between the nearest surfaces and between the interface with its nearest surfaces can be eliminated. In general, the necessary thickness of the vacuum region is $\sim 10$ Å, while the thickness of every slab depends on its structure properties.

To construct a slab model of tractable size, the misfit between the rutile and anatase surface has to be considered. The area $A$ of the interface is chosen to keep the conservation of periodicity of both parent slabs. Hence, the length and width of the simulation box are the least common multiples of the length and width of unit cells in both phases. Using the near-coincidence-site lattice (NCSL) theory, I could calculate the area $A$ of the interface satisfying the relationship [96, 97]

$$A = n_{\rm a}a_{\rm a} \times m_{\rm a}b_{\rm a} \approx n_{\rm r}a_{\rm r} \times m_{\rm r}b_{\rm r}, \tag{5.1}$$

where $n_{\rm a}, m_{\rm a}, n_{\rm r}, m_{\rm r}$ are adjustable parameters. The lattice parameters are taken from experiment of rutile $a_{\rm r}$=4.587 Å and $b_{\rm r}$= 2.954 Å, and of anatase $a_{\rm a}$= 3.782 Å and $b_{\rm a}$=9.502 Å, respectively.

In fact, two slabs cannot match perfectly, I have introduced a misfit deformation into the system (shrinking or stretching the slabs in order to get the same area). The misfit percentage values along the length and width of the interface are defined as

$$M_{\rm m} = \Big(1 - \frac{m_{\rm a}a_{\rm a}}{m_{\rm r}a_{\rm r}}\Big)100, \qquad M_{\rm n} = \Big(1 - \frac{n_{\rm a}a_{\rm a}}{n_{\rm r}a_{\rm r}}\Big)100. \tag{5.2}$$

The stability of the interface can be expressed by the adhesion energy $E_{\rm adh}$, which is defined as the energy needed (per unit area) to reversibly separate the two phases. Formally, $E_{\rm adh}$ can be defined as the total energy difference between the slab containing the interface and two isolated slabs

$$E_{\rm adh} = \frac{E_{\rm interface} - E_{\rm a}^{\rm slab} - E_{\rm r}^{\rm slab}}{A}. \tag{5.3}$$

Here $E_{\rm interface}$ is the total energy of the interface system, $E_{\rm a}^{\rm slab}$ and $E_{\rm r}^{\rm slab}$ are the total energies of anatase and rutile slabs, respectively.

Recently, Deskins *et al.* [98] have performed classical force field calculations for

Table 5.1: The adhesion energies $E_{\mathrm{adh}}$ of interfaces formed by rutile and anatase surfaces. The $a_{\mathrm{r}} \times b_{\mathrm{r}}, a_{\mathrm{a}} \times b_{\mathrm{a}}, M_{\mathrm{m}}, M_{\mathrm{n}}$ are the surface sizes and corresponding to misfit values.

| Rutile/Anatase | $a_{\mathrm{r}} \times b_{\mathrm{r}}/a_{\mathrm{a}} \times b_{\mathrm{a}}$ NCSL | $M_{\mathrm{m}}$ (%) | $M_{\mathrm{n}}$ (%) | $E_{\mathrm{adh}}$ $(J/m^2)$ |
|---|---|---|---|---|
| r(100)/a(100) (Ref. [98]) | 36/14 | 3.47 | -0.68 | -2.82 |
| r(110)/a(101) (Ref. [98]) | 99/49 | 0.40 | -0.41 | -1.71 |
| r(100)/a(100) (My model) | $2 \times 4/3 \times 1$ | 3.45 | -4.14 | -1.54 |

many interfaces between rutile and anatase. They have found the interface between rutile(100) and anatase(100) to have the highest adhesion energy. Therefore, in this thesis, I concentrated the band alignment across this interface. According to the NCSL theory, a rutile[2x4]/anatase[3x1] slab model (i.e. 8 rutile and 3 anatase surface units) of the rutile(100)/anatase(100) inteface will have a misfit of $\sim 4\%$ in both directions. Such a slab model with layer thicknesses of rutile 13.761 Å and anatase 15.128 Å contains 288 atoms and is still tractable by ab initio calculation. In comparison, the slab of Deskins, containing 36 rutile and 14 anatase surface units has still 3.47% misfit in one direction. The interface between the most stable surface, rutile(110) and anatase(101) would require even a bigger slab.

Aligning two slabs allows various initial configurations of the interface. I have constructed the initial configuration to ensure the highest possible degree of the stoichiometry at the interface. The anatase (100) surface is a polar, so I cut the rutile(100) slab in such a way that its surface because nearly a polar too. This initial configuration (Figure 5.2 - left side) was subjected to simulated annealing , in order to get a usable model of the actual rutile(100)/anatase(100) interface. The annealing was carried out by constant volume molecular dynamics (using the DFTB+ code [99]), i.e. with the outer double layers on both sides of the slab fixed. First, the system (all together 228 atoms) was heated up to 1000K in the linear ramp of 5ps, held there for 20ps and the cooked back to 0K with an exponential ramp of 5ps. The resulting

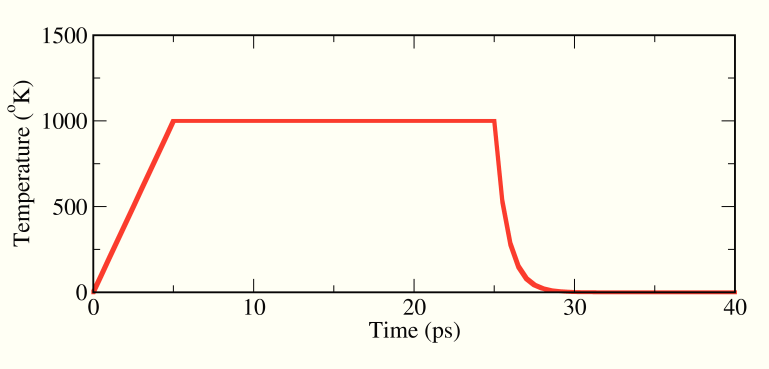


Figure 5.1: Diagram of rutile(100)/anatase(100) interfaces DFTB-MD. The system was heated up to 1000K in the linear ramp of 5ps, held there for 20ps and the cooked back to 0K with an exponential ramp of 5ps.

Table 5.2: The lattice parameters of anatase and rutile from experiment, NCSL theory (shrinking or stretching the slabs), and optimization

| Interface r(100)/a(100) | | Experiment | NSCL theory | optimization |
|---|---|---|---|---|
| Anatase | $a$(Å) | 3.782 | 3.860 | **3.872** |
| | $c$(Å) | 9.502 | 9.338 | **9.364** |
| Rutile | $a$(Å) | 4.587 | 4.669 | **4.682** |
| | $c$(Å) | 2.954 | 2.895 | **2.904** |

structure was the extended on both sides by perfect crystalline layers of the same larval size as the slab, so both the rutile and the anatase part were doubled in thickness. This increased system (all together 576 atoms) was the relaxed at 0K using ab initio PBE, without any constraint. Table 5.2 presents the average lattice parameters of the anatase and rutile phase in the optimized interface model.

The final interface rutile(100)/anatase(100) is shown in Figure 5.2 (right side). The interface picture suggests that there is some disorder at the first rutile layer while there is no big change in the anatase slab. At the interface, the 5 fold-coordinated titanium atoms of the anatase surface make bonds with 2 fold-coordinated oxygen atoms of the rutile surface. There is a strong binding between two slabs, mainly by tetrahedral $TiO_4$ which have been observed in the UV/Vis diffuse reflectance and XAFS measurement. [100]

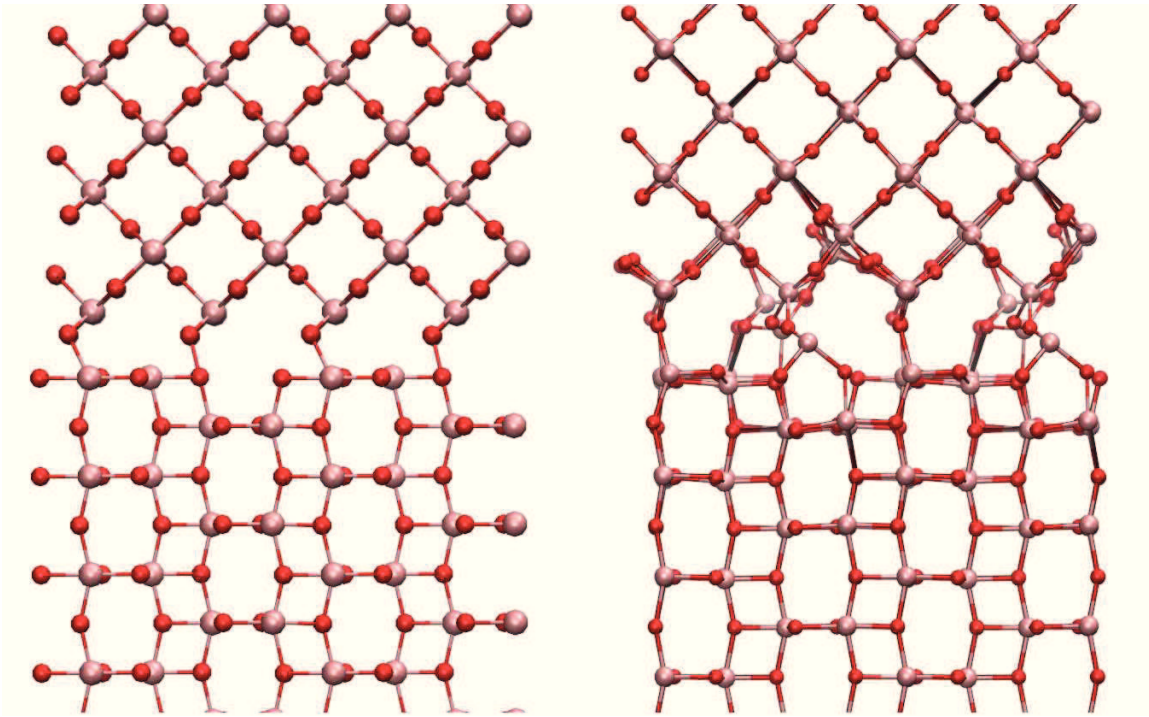

Figure 5.2: Initial slab model (left) and last optimized interface (right side) between rutile(100) and anatase(100). Big gray and small red circles indicate the titanium and oxygen atoms, respectively.

## 5.2 Band line-up across rutile(100)/anatase(100)

In oder to determine the band alignment of anatase(100)/rutile(100) interface, I have used the technique introduced by Van de Walle and Martin [101]. This consists three calculations: interface calculation and two bulk calculations of rutile and anatase. The interface calculation gives a jump of an average electrostatic potential across the interface while two bulk calculations locate the band edges with respect to the respective average electrostatic potential of each phase.

The average potential $\bar{V}(z)$ in the plane $(x, y)$ parallel to the interface is given by

$$\bar{V}(z) = \frac{1}{NA} \int V(\mathbf{r}) dxdy, \tag{5.4}$$

where $A$ is the area of the planes, N is the number of the taken planes.

The jump of average potential across rutile(100)/anatase(100) is shown in Figure 5.3. The layers far from the surfaces and the interface converge to their bulk value. The potentials of bulk anatase and rutile are matched to the figures to determine the average potential of each slab. I found the jump $\Delta\bar{V}(z) = \bar{V}(z)_{\text{rutile}} - \bar{V}(z)_{\text{anatase}}$ = 0.13 eV. Note that from this calculation, the band line-up can be determined directly from the DOS (Figure 5.4). However, it is difficult to measure and the PBE calculation gives both the valence band and conduction band on the wrong place.

Since PBE describes the ground state well, I have used the PBE potential jump, which was calculated from the actual inteface, to align the HES06 bulk band structures. From the Figure 5.5, I found that the CB-offset is about 0.46 eV, while the VB-offset is 0.67 eV, with rutile being higher. This result corroborates the generic value of 0.3 - 0.4 eV obtained earlier without explicity taking into account any interface. [51]. As a result, electrons exited by the light move from the rutile to anatase phase while holes move in the opposite direction.

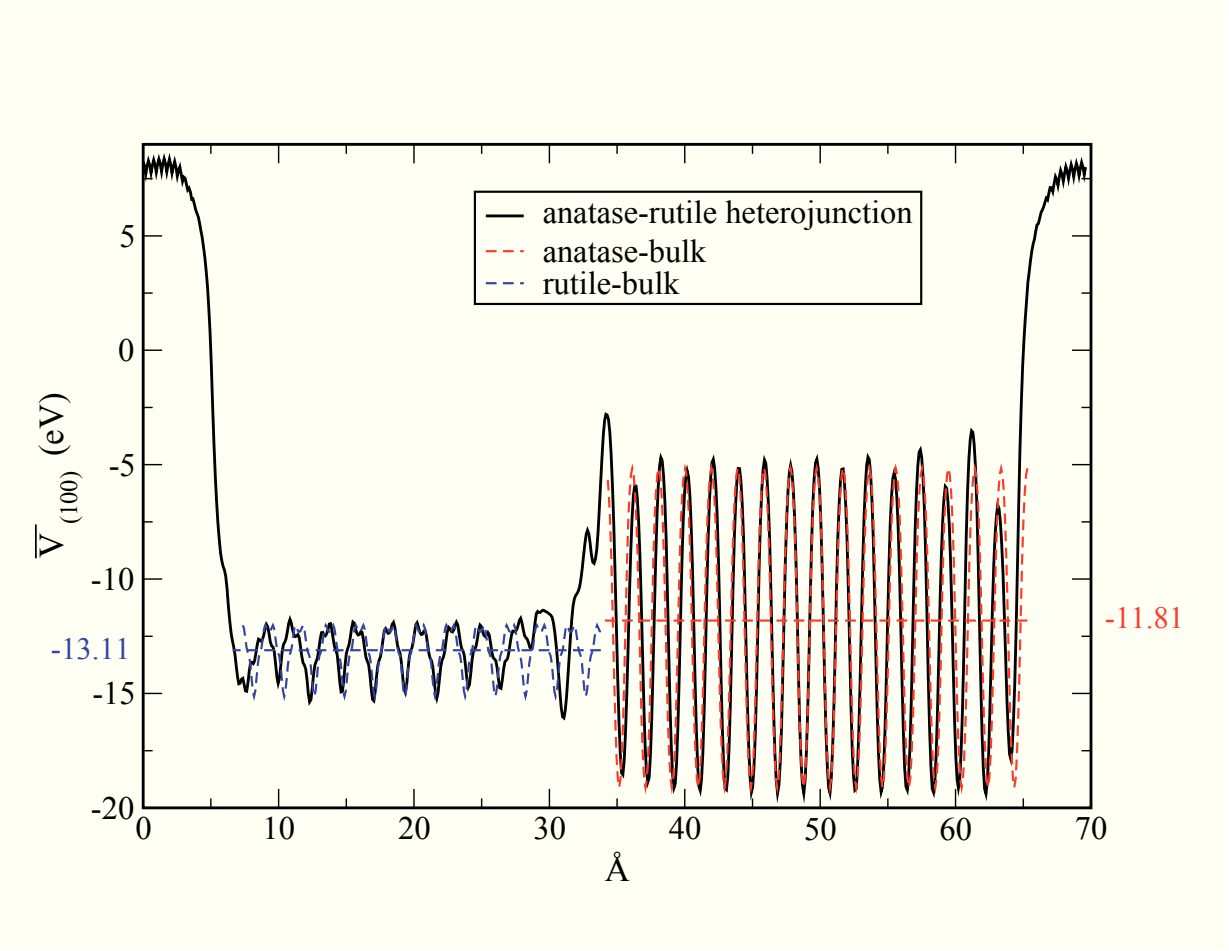


Figure 5.3: Variation of the averaged potential across the interface. The dash red lines and dash blue lines show the corresponding potential for bulk anatase and bulk rutile. The shift between $\bar{V}_{\text{anatase}}$ and $\bar{V}_{\text{rutile}}$ determines the band line-up.

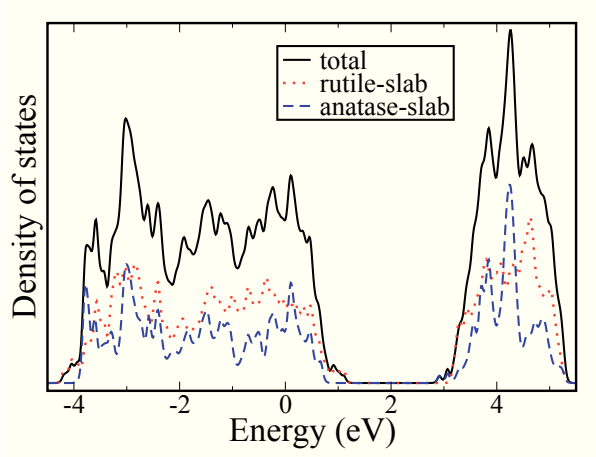


Figure 5.4: DOS of rutile(100)/anatase(100) heterojuntions in PBE. The black solid, red dotted, blue dashed lines denote the total DOS of interface, and separated individual rutile, and anatase slabs, correspondingly.

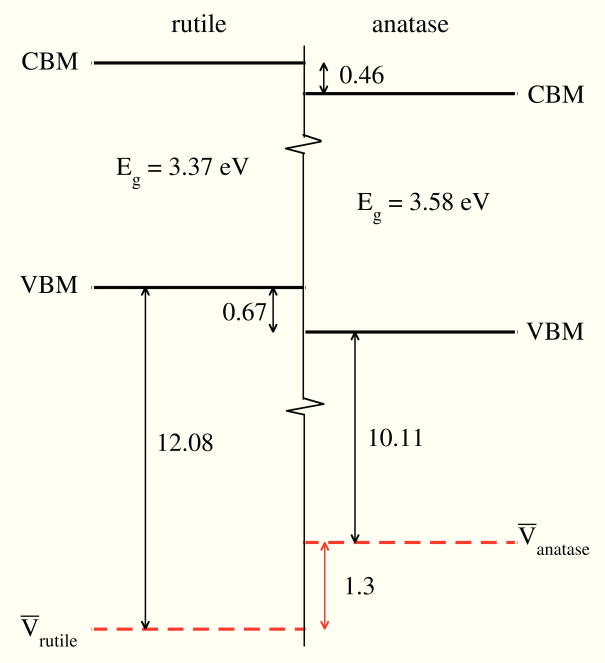


Figure 5.5: Derivation of band lineups: relative position of the average potentials $\bar{V}_{anatase}$ and $\bar{V}_{rutile}$ and of the anatase and rutile valence and conduction bands in HSE

# CHAPTER VI

# Conclusion

## 6.1 Work performed

### 6.1.1 Nb- and Ta-doped anatase for the TCO application

In this thesis, I have performed calculations for the band structures of Nb- and Ta- doped bulk anatase. My calculations, which are based on the density functional theory and both the PBE and HSE06 functionals for the exchange energy, show that these materials are both suitable for the TCO application. In particular, beside the necessary transparency, highly doped anatase behaves like a metal because Nb- and Ta-dopants release their extra electrons to the bottom of the conduction band of host atoms.

A method to calculate the optical effective mass using finite difference technique is also developed in this thesis. The integral of $\nabla_{\mathbf{k}}\varepsilon(\mathbf{k})$ is calculated over the Fermi surface, using the $\varepsilon(\mathbf{k})$ function fitted to the ab initio electronic structure calculated at the discrete k-points. By determining the Fermi energy from the calculated band structure, I was able to compute the optical effective mass at different concentrations. As a result, my HSE06 results agree very well with the experimentally observed concentration dependence. An analysis on the results reveals that at the relevant concentrations for the TCO application, the complicated concentration dependence

of the optical effective mass is a consequence of the population of the secondary minimum in the CB of anatase.

The optical effective mass determined from my calculations is highly anisotropic, specifically $m_{\parallel} \gg m_{\perp}$ for both Ta-doped and Nb-doped anatase. The anisotropy in the Ta-doped anatase is smaller, roughly a half of that in the Nb-doped anatase. The solubility of the Ta dopant is higher than that of the Nb dopent, Ta should be the preferred dopant for the TCO application.

An analysis on the heat of formation is given, clearly explaining the role of a reducing atmosphere for efficient dopant incorporation. In contrast to earlier assumptions in the literature, my result indicates that oxygen vacancies play no role in the process of dopant incorporation.

### 6.1.2 $TiO_2$ nanowires and Nb- and Ta-doping in anatase wires

My work on $TiO_2$ nanotructures (with B. Aradi) shows that the [001]-anatase nanowires are stabilized by the presence of a screw axis (nonsymomorphic line group with point group $D_4$). Such wires doped by Nb and Ta are also investigated. Similar to the bulk case, The dopants in the anatase nanowires also give their extra electrons to the bottom of the conduction bands of the nanowires. The most favorable sites for the dopants are the fully coordinated sub-corner Ti sites because of their low formation energies. The dopants incorporation into the preferable sites, which are connected to the symmetry of the doped NWs, clearly explaining that the conduction band of high symmetric NWs is hardly perturbed by doping.

### 6.1.3 Band alignment across the anatase(100)/rutile(100) interface

To calculate the band off-set of the anatase/rutile with the highest adhension energy, I have built a slab model of the interface. The slab model was exposed to simulated annealing by SCC-DFTB molecular simulations, and then relaxed by *ab*

*initio* calculations with the PBE functional at 0K. From the PBE calculations, I have determined the jump of the layer-averaged electrostatic potential across a(100)/r(100) interface. This value was then used to align the band structures of the bulk rutile and anatase. From my HSE06 calculations, the offset of the anatase was determined to be 0.46 eV, while that of the rutile is higher. Therefore, the electrons excited by light will move from the rutile to the anatase in a mixtured powder while the holes accumulate in rutile. Consequently, the electron-hole recombination will be decreased, and the mixture phase will have a higher photocatalytic activity than the single phases.

## 6.2 Future development

In Chapter 3, I have shown the important role of $n-$type doping in the anatase for the TCO applications. However, $p-$type doping in $TiO_2$ might also be possible, thus opening new ways for the transparent electronics. Recently, by using the HSE06 functional, Deák *et al.* have found that in agreement with experimental results for Al-doped samples, polaronic hole states (self-trapping of the acceptor hole) occur only in anatase, while all cation site acceptors have EMT states in rutile. [102] Therefore, in the next stage, I will start calculations for the optical effective mass of Al-doped rutile by using the same finite difference techniques used for Nb- and Ti-doped anatase. On the other hand, various interfaces between the anatase and the rutile phases will also be investigated. In particular, as discussed in Chapter 5, although the band alignment of the anatase(100)/rutile(100) interface was found to have the highest adhesion energy, several other specific interfaces on suitable model can be proposed. For example, in contrast to the the most reactive surface, the anatase(101)/rutile(110) interface, which is the most stable surface, can be investigated to clarify the issue of charge separation.

# APPENDIX A

In doped anatase, an energy function $\varepsilon^{\ell}(\mathbf{k})$ can be fitted from a given band structure in the branch $\ell$. However, the function may contain a term $|k_z|$ (see equation (3.1)). The first derivative of this term is constant everywhere and discontinuous at $k_z = 0$ leading to an undefined second derivative of the energy function which determines the optical effective mass by equation (2.38). For example, at high Ta-dopant fraction ($x = 0.063$), three Fermi surfaces $S^{\ell}_{\varepsilon_{\mathrm{F}}}$ given by $\varepsilon^{\ell}(\mathbf{k}) = \varepsilon_{\mathrm{F}}$ contribute to the optical effective mass (Figure A.1). To determine the optical effective mass, we can calculate from the surface integral (2.37) and separate it into 2 integrals at the discontinuous plane $k_z = 0$. The integral in equation (2.37) can be written by

$$I = \int\limits_{S^{+}_{\varepsilon^{\ell}_{F}}} \nabla\varepsilon^{\ell} d\mathbf{S}^{\ell} + \int\limits_{S^{\ell+}_{0}} \nabla\varepsilon^{\ell}\Big|_{k_z^{+}=0} d\mathbf{S}^{\ell}_{0} + \int\limits_{S^{-}_{\varepsilon^{\ell}_{F}}} \nabla\varepsilon^{\ell} d\mathbf{S}^{\ell} + \int\limits_{S^{\ell-}_{0}} \nabla\varepsilon^{\ell}\Big|_{k_z^{-}=0} d\mathbf{S}^{\ell}_{0}. \tag{A.1}$$

Introducing $\mathbf{n}^{\ell+} = (0, 0, -1)$ and $\mathbf{n}^{\ell-} = (0, 0, 1)$ as normal unit vectors of surfaces $S^{\ell+}_{0}$ and $S^{\ell-}_{0}$ to the integral, we get

$$I = \int\limits_{S^{\ell}_{\varepsilon_{F}}} \nabla\varepsilon^{\ell} d\mathbf{S}^{\ell} + \int\limits_{S^{\ell+}_{0}} \nabla\varepsilon^{\ell}\Big|_{k_z^{+}=0} . \mathbf{n}^{\ell+} dk_x dk_y + \int\limits_{S^{\ell-}_{0}} \nabla\varepsilon^{\ell}\Big|_{k_z^{-}=0} . \mathbf{n}^{\ell-} dk_x dk_y. \tag{A.2}$$

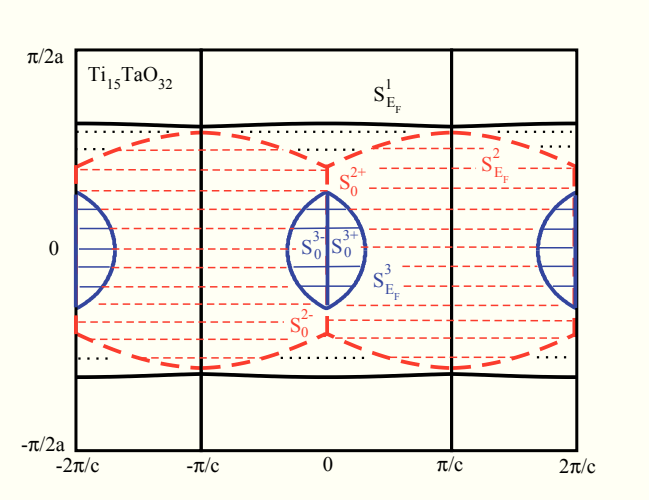


Figure A.1: Fermi surfaces of the anatase with high Ta-dopant fraction of $x = 0.063$ in repeated-BZ plane. Unclosed thick solid black and dashed red curves are Fermi surfaces of the first and second HSE06 CBs, respectively. Closed thick solid blue curve is Fermi surface made by the third HSE06 CBs. Thick dashed red and solid blue linear lines at $(k_z = 0, \pm 2\pi/c)$-plane are $S_0^{2\pm}$ $S_0^{3\pm}$ surfaces dividing k-space inside the Fermi surfaces. $a$ and $c$ are the lattice parameters of the anatase unit cell.

Expanding two dot products,

$$\nabla\varepsilon^{\ell}\Big|_{k_z^+=0}.\mathbf{n}^{\ell+} = (\frac{\partial\varepsilon^{\ell}}{\partial k_x}\Big|_{k_z^+=0}, \frac{\partial\varepsilon^{\ell}}{\partial k_y}\Big|_{k_z^+=0}, \frac{\partial\varepsilon^{\ell}}{\partial k_z}\Big|_{k_z^+=0})(0,0,-1) = -a_7 - a_9(k_x^2+k_y^2), \quad \text{(A.3)}$$

$$\nabla\varepsilon^{\ell}\Big|_{k_z^-=0}.\mathbf{n}^{\ell-} = (\frac{\partial\varepsilon^{\ell}}{\partial k_x}\Big|_{k_z^-=0}, \frac{\partial\varepsilon^{\ell}}{\partial k_y}\Big|_{k_z^-=0}, \frac{\partial\varepsilon^{\ell}}{\partial k_z}\Big|_{k_z^-=0})(0,0,-1) = -a_7 - a_9(k_x^2+k_y^2), \quad \text{(A.4)}$$

we can rewrite the integral in form

$$I = \int\limits_{S_{\varepsilon_F^{\ell}}} \nabla\varepsilon^{\ell} d\mathbf{S} + 2\int\limits_{S_0^{\ell}} [-a_7 - a_9(k_x^2+k_y^2)]dk_x dk_y. \quad \text{(A.5)}$$

Here, the second part in equation (A.5) presents the contribution of the $|k_z|$ term to the reduction of parallel optical effective mass while the first one can be written as

$$\int\limits_{S_{\varepsilon_F^{\ell}}} \nabla\varepsilon d\mathbf{S} = \int\limits_{T_{\varepsilon_F}^x} \frac{\partial\varepsilon}{\partial k_x}dk_y dk_z + \int\limits_{T_{\varepsilon_F}^y} \frac{\partial\varepsilon}{\partial k_y}dk_z dk_x + \int\limits_{T_{\varepsilon_F}^z} \frac{\partial\varepsilon}{\partial k_z}dk_x dk_y, \quad \text{(A.6)}$$

where $T^x_{\varepsilon_F}, T^y_{\varepsilon_F}, T^z_{\varepsilon_F}$ are projections of Fermi surface $S_{\varepsilon_F}$ into yz-, zx-, and xy-planes, respectively.

Combining equation (2.37), (A.5) and (A.6), I define the optical effective mass as

$$\frac{1}{m_{\text{opt}}} = \frac{1}{m_x} + \frac{1}{m_y} + \frac{1}{m_z}, \tag{A.7}$$

with the othogonal optical effective masses

$$\frac{1}{m_x} = \frac{2}{(2\pi)^3 \hbar n_e} \sum_\ell \int\limits_{T^x_{\varepsilon_F}} \frac{\partial \varepsilon^\ell}{\partial k_x} dk_y dk_z, \qquad \frac{1}{m_y} = \frac{2}{(2\pi)^3 \hbar n_e} \sum_\ell \int\limits_{T^y_{\varepsilon_F}} \frac{\partial \varepsilon^\ell}{\partial k_y} dk_z dk_x, \tag{A.8}$$

and the parallel one

$$\frac{1}{m_z} = \frac{2}{(2\pi)^3 \hbar n_e} \sum_\ell \Big[ \int\limits_{T^z_{\varepsilon_F}} \frac{\partial \varepsilon^\ell}{\partial k_z} dk_x dk_y + 2 \int\limits_{S^\ell_0} [-a_7 - a_9(k_x^2 + k_y^2)] dk_x dk_y \Big]. \tag{A.9}$$

In case of continuous energy function, calculating from equation (A.2), we have

$$\int\limits_{S^{\ell+}_0} \nabla \varepsilon^\ell \Big|_{k_z^+ = 0} \mathbf{n}^+ dk_x dk_y + \int\limits_{S^{\ell-}_0} \nabla \varepsilon^\ell \Big|_{k_z^- = 0} \mathbf{n}^- dk_x dk_y = 0. \tag{A.10}$$

The parallel term now is formed

$$\frac{1}{m_z} = \frac{2}{(2\pi)^3 \hbar n_e} \sum_\ell \int\limits_{T^z_{\varepsilon_F}} \frac{\partial \varepsilon^\ell}{\partial k_z} dk_x dk_y. \tag{A.11}$$

The optical effective mass calculated by equation (2.38) is now similar to that done by equation (2.37) in Gauss theory application.

# Bibliography


[1] H. A. Huy, B. Aradi, T. Frauenheim, and P. Deák. Calculation of carrier-concentration-dependent effective mass in Nb-doped anatase crystals of $TiO_2$. *Phys. Rev. B*, 83:155201, 2011.

[2] H. A. Huy, B. Aradi, T. Frauenheim, and P. Deák. Comparison of Nb- and Ta-doping of anatase $TiO_2$ for transparent conductor applications. *J. Appl. Phys.*, 112:016103, 2012.

[3] B. Aradi, P. Deák, H. A. Huy, A. Rosenauer, and Th. Frauenheim. Role of symmetry in the stability and electronic structure of titanium dioxide nanowires. *J. Phys. Chem. C*, 115:18494–18499, 2011.

[4] P. Deák, B. Aradi, A. Gagliardi, G. Penazzi, H. A. Huy, T. Wehling, B. Yan, and T. Frauenheim. *in preparation*, 2012.

[5] H. A. Huy, B. Aradi, T. Frauenheim, and P. Deák. Charge Seperation in Photocatalysis of Rutile-Anatase Interfaces. *in preparation*, 2012.

[6] T. Tsukada. Active-matrix liquid-crystal displays, in: R.A. Street (Ed.), technology and application of amorphous silicon. *Springer, Berlin, Germany*, 37:7–89, 2000.

[7] D. S. Ginley and C. Bright. Transparent conducting oxides. *MRS Bull.*, 25:15–18, 2000.

[8] D. Metzdorf, E. Becker, T. Dobbertin, S. Hartmann, D. Heithecker, H. Johannes, A. Kammoun, H. Krautwald, T. Riedl, C. Schildknecht, D. Schneider, and W. Kowalsky. OLED matrix-displays. *Mater. Res. Soc. Symp. Proc.*, 769:H.4.2.1, 2003.

[9] N. G. Dhere. Toward GW/year of CIGS production within the next decade. *Sol. Ene. Ma.& Sol. Cell*, 91:1376–1382, 2007.

[10] T. Hitosugi, N. Yamada, S. Nakao, Y. Hirose, and T Hasegawa. Properties of $TiO_2$-based transparent conducting oxides. *Phys. Status Solidi A*, 207:1529–1537, 2010.

[11] P. Canhola, N. Martins, L. Raniero, S. Pereira, E. Fortunato, I. Ferreira, and R. Martins. Role of annealing environment on the performances of large area ITO films produced by RF magnetron sputtering. *Thin Solid Films*, 487:271–276, 2005.

[12] K. Ellmer. Resistivity of polycrystalline zinc oxide films: current status and physical limit. *J. Phys. D: Appl. Phys.*, 34:3097–3108, 2001.

[13] T. Minami. Transparent conducting oxide semiconductors for transparent electrodes. *Semicond. Sci. Technol.*, 20:S35–S44, 2005.

[14] T. Minami. New $n$-Type Transparent Conducting Oxides. *MRS Bull.*, 38:38–44, 2000.

[15] T. Minami, H. Sato, H. Imamoto, and S. Takata. Substrate Temperature Dependence of Transparent Conducting Al-Doped ZnO Thin Films Prepared by Magnetron Sputtering. *Jpn. J. Appl. Phys.*, 31:L257–L260, 1992.

[16] Y. Furubayashi, T. Hitosugi, Y. Yamamoto, K. Inaba, G. Kinoda, Y. Hirose, T. Shima, and Hasegawa. A transparent metal: Nb-doped anatase $TiO_2$. *Appl. Phys. Lett.*, 86:252101, 2005.

[17] Y. Furubayashi, T. Hitosugi, Y. Yamamoto, Y. Hirose, G. Kinoda, K. Inaba, T. Shimada, and T. Hasegawa. Novel transparent conducting oxide: Anatase $Ti_{1-x}Nb_xO_2$. *Thin Solid Film*, 496:157–159, 2006.

[18] M. A. Gillispie, M. F.A.M. van Hest, M. S. Dabney, J. D. Perkin, and D. S. Ginley. Sputtered Nb- and Ta-doped $TiO_2$ transparent conducting oxide films on glass. *J. Mater. Res.*, 22:2832–2837, 2007.

[19] B. Neumann, F. Bierau, B. Johnson, C. A. Kaufmann, K. Ellmer, and H. Tributsch. Niobium-doped $TiO_2$ films as window layer for chalcopyrite solar cells. *Phys. Stat. Sol.*, 245:1849–1857, 2008.

[20] X. T. Zhang, O. Sato, M. Taguchi, Y. Einaga, T. Murakami, and A. Fujishima. Self-Cleaning Particle Coating with Antireflection Properties. *Chem. Mater.*, 17:696–700, 2005.

[21] M. Ni, M. K.H. Leung, D. Y.C. Leung, and K. Sumathy. A review and recent developments in photocatalytic water-splitting using $TiO_2$ for hydrogen production. *Renew. Sustain. Energy Rew.*, 11:401–425, 2007.

[22] T. Hitosugi, H. Kamisaka, K. Yamashita, H. Nogawa, Y. Furubayashi, S. Nakao, N. Yamada, A. Chikamatsu, H. Kumigashira, M. Oshima, Y. Hirose, T. Shimada, and T. Hasegawa. Electronic band structure of transparent conductor: Nb-doped anatase $TiO_2$. *Appl. Phys. Express*, 1:111203, 2008.

[23] H. Kamisaka, T. Hitosugi, T. Suenaga, T. Hasegawa, and K. Yamashita. Density functional theory based first-principle calculation of Nb-doped anatase $TiO_2$ and its interactions with oxygen vacancies and interstitial oxygen. *J. Chem. Phys.*, 131:034702, 2009.

[24] M. Mikami, S. Nakamura, O. Kitao, H. Arakawa, and X. Gonze. First-principles study of titanium dioxide: Rutile and anatase. *Jpn. J. Appl. Phys., Part 2*, 39:L847–L850, 2000.

[25] R. Asahi, Y. Taga, W. Mannstadt, and A. J. Freeman. Electronic and optical properties of anatase $TiO_2$. *Phys. Rev. B*, 61:7459–7465, 2000.

[26] P. P. Edwards, A. Porch, M. O. Jones, D. V. Morgan, and R. M. Perks. Basic materials physics of transparent conducting oxides. *Dalton Trans.*, 2004:2995–3002, 2004.

[27] Y. Furubayashi, N. Yamada, Y. Hirose, Y. Yamamoto, M. Otani, T. Hitosugi an T. Shimada, and T. Hasegawa. Transport properties of d-electron-based transparent conducting oxide: Anatase $Ti_{1-x}Nb_xO_2$. *J. Appl. Phys.*, 101:093705, 2007.

[28] Y. Hirose, N. Yamada, S. Nakao, T. Hitosugi, T. Shimada, and T. Hasegawa. Large electron mass anisotropy in a d-electron-based transparent conducting oxide: Nb-doped anatase $TiO_2$ epitaxial films. *Phys. Rev. B*, 79:165108, 2009.

[29] T. Hitosugi, Y. Furubayashi, A. Ueda, K. Itabashi, K. Ina, Y. Hirose, G. Kinoda, Y. Yamamoto, T. Shimada, and T. Hasegawa. Ta-doped anatase $TiO_2$ epitaxial film as transparent conducting oxide. *Jpn. J. Appl. Phys., Part 2*, 44:L1063–L1065, 2005.

[30] J. O. Guillén, S. Lany, and A. Zunger. Atomic control of conductivity versus ferromagnetism in wide-gap oxides via selective doping: V, Nb, Ta in anatase $TiO_2$. *Phys. Rev. Lett.*, 100:036601, 2008.

[31] A. R. Barman, M. Motapothula, A. Annadi, K. Gopinadhan, Y. L. Zhao, Z. Yong, I. Santoso, Ariando, M. Breese, A. Rusydi, S. Dhar, and T. Venkatesan. Multifunctional $Ti_{1x}Ta_xO_2$: Ta doping or alloying? *Appl. Phys. Lett.*, 98:072111, 2011.

[32] T. Yamamoto and T. Ohno. Screened hybrid density functional study on Nb- and Ta-doped $TiO_2$. *Phys. Rev. B*, 85:033104, 2012.

[33] T. Hitosugi, A. Ueda, S. Nakao, N. Yamada, Y. Furubayashi, Y. Hirose, T. Shimada, and T. Hasegawa. Fabrication of highly conductive $Ti_{1x}Nb_xO_2$ polycrystalline films on glass substrates via crystallization of amorphous phase grown by pulsed laser deposition. *Appl. Phys. Lett.*, 90:212106, 2007.

[34] S. Daothong, N. Songmee, S. Thongtem, and P. Singjai. Size-controlled growth of $TiO_2$ nanowires by oxidation of titanium substrates in the presence of ethanol vapor. *Scripta Mater.*, 57:567–570, 2007.

[35] J. Jitputti, Y. Suzuki, and S. Yoshikawa. Synthesis of $TiO_2$ nanowires and their photocatalytic activity for hydrogen evolution. *Catal. Commun.*, 9:1265–1271, 2008.

[36] Y. Lin. Photocatalytic activity of $TiO_2$ nanowire arrays. *Mater. Lett.*, 62:1246–124, 2008.

[37] S. Yang C. Liu. Synthesis of angstrom-scale anatase titania atomic wires. *ACS Nano*, 3:1025–1031, 2009.

[38] D. Zhang, P. Liu, and C. Liu. Thinnest titanium dioxide nanowires assembled by $Ti_2O_4$ building blocks. *J. Phys. Chem. C*, 112(43):16729–16732, 2008.

[39] I. Amilcare, C. Giovanni, T. Fabio, and N. Domenico. DFT Study on Anatase $TiO_2$ Nanowires: Structure and Electronic Properties As Functions of Size, Surface Termination, and Morphology. *Journal of Physical Chemistry C*, 114(29):12389–12400, 2010.

[40] A. Fujishima and K. Honda. Electrochemical photolysis of water at a semiconductor electrode. *Nature*, 238:37–38, 1972.

[41] R. Asahi, T. Morikawa, T. Ohwaki, K. Aoki, and Y. Taga. Visible-light photocatalysis in nitrogen-doped titanium oxides. *Science*, 294:269–271, 2001.

[42] M. K. Seery, R. George, P. Floris, and S. C. Pillai. Silve oped titanium doxides nanomaterials for enhanced visible light photocatalysis. *J. Photochem. Photobio. A: Chem.*, 189:256–263, 2007.

[43] U. Gesenues. *Faber & Lack*, 100:244, 1994.

[44] R. I. Bickley, T. Gonzalez-Carreno, J. S. Lees, L. Palmisanod, and R. J. D. Tilley. As structural investigation of titanium dioxide photocatalysts. *J. Solid. State Chem.*, 92(1):178–190, 1991.

[45] Y. K. Kho, A. Iwase, W. Y. Teoh, L Mädler, A. Kudo, and R. Amal. Photocatalytic $H_2$ evolution over $TiO_2$ nanoparticles. The Synergistic Effect of Anatase and Rutile. *J. Phys. Chem. C*, 114:2821–2829, 2010.

[46] K. A. Gray T. Rajh M. C. Thurnauer D. C. Hurum, A. G. Agrios. Explaining the Enhanced Photocatalytic Activity of Degussa P25 Mixed-Phase $TiO_2$ using EPR. *J. Phys. Chem. B*, 107:4545–4549, 2003.

[47] S. E. Crist K. A. Gray T. Rajh M. C. Thurnauer D. C. Hurum, A. G. Agrios. Probing reaction mechanism in mixed-phase $TiO_2$ by EPR. *J. Elec. Spec. Rel. Phe.*, 150:155–163, 2006.

[48] H. Nakajima, Q. Shen T. Mori, and T. Toyoda. Photoluminescence study of mixtures of anatase and rutile $TiO_2$ nanoparticles: Influence of charge transfer between the nanoprticles on their photoluminesence excitation bands. *Chem. Phys. Lett.*, 409:81–84, 2005.

[49] R. G. Nair, S. Paul, and S. K. Samdarshi. High UV/visible light activity of mixed phase titania: Ageneric mechanism. *Sol. Ene. Ma.& Sol. Cell*, 95:1901–1907, 2011.

[50] R. Scotti, I. R. Bellobono, C. Canevali, C. Cannas, M. Catti, M. D. Arienzo, A. Musinu, S. Polizzi, M. Sommariva, A. Testino, and F. Morazzoni. Solgel pure and mixed-phase titanium dioxide for photocatalytic purposes: relations between phase composition, catalytic activity, and charge-trapped sites,. *Chem. Mater*, 20:4051–4061, 2008.

[51] P. Deák, B. Aradi, and Th. Frauenheim. Band lineup and charge carrier separation in mixed rutile-anatase systems. *J. Phys. Chem.*, 115(8):3443–3446, 2011.

[52] A. Schleife, F. Fuchs, C. Rdl, J. Furthmller, and F. Bechstedt. Branch-point energies and band discontinuities of III-nitrides and III-/II-oxides from quasiparticle band-structure calculations. *Appl. Phys. Lett.*, 94:012104, 2009.

[53] M. Born and R. Oppenheimer. Zur Quantentheorie der Molekeln. *Ann. Phys.*, 389(2):457–484, 1927.

[54] P. Hohenberg and W. Kohn. Inhomogeneous Electron Gas. *Phys. Rev.*, 136:B864, 1964.

[55] W. Kohn and L.Sham. Self-Consistent Equations Including Exchange and Correlation Effects. *Phys. Rev.*, 140:A1133–A1138, 1965.

[56] R. G. Parr and W. Yang. *Density Functional Theory of Atoms and Molecules*. Oxford University Press, Oxford, 1989.

[57] J. P. Perdew and L. Burke. Comparison shopping for a gradient-corrected density functional. *Int. J. Quant. Chem.*, 57:309–319, 1996.

[58] J. P. Perdew and Y. Wang. Accurate and simple analytic representation of the electron-gas correlation energy. *Phys. Rev. B*, 45:13244–13249, 1992.

[59] A. D. Becke. Density-functional exchange-energy approximation with correct asymptotic behavior. *Phys. Rev. A*, 38:3098–3100, 1988.

[60] J. P. Perdew, K. Burke, and M. Ernzerhof. Generalized gradient approximation made simple. *Phys. Rev. Lett.*, 77(18):3865–3868, 1996.

[61] S. Kümmel and L. Kronik. Orbital-dependent density functionals: Theory and applications. *Rev. Mod. Phys.*, 80:3–58, 2008.

[62] P. Deák, B. Aradi, Th. Frauenheim, E. Janzen, and A. Gali. Accurate defect levels obtained from the HSE06 range-separated hybrid functional. *Phys. Rev. B*, 81:153203, 2010.

[63] H. Tang, K. Prasad, R. Sanjinès, P. E. Schmid, and F. Lévy. Electrical and optical properties of $TiO_2$ anatase thin films. *J. Appl. Phys.*, 75:2042–2047, 1994.

[64] B. J. Morgan, D. O. Scanlon, and G. W. Watson. Small polarons in Nb- and Ta rutile and anatase $TiO_2$. *J. Mater. Chem.*, 19:5175–5178, 2009.

[65] S. Lany and A. Zunger. Polaronic hole localization and multiple hole binding of acceptors in oxide wide-gap semiconductors. *Phys. Rev. B*, 80:085202, 2009.

[66] S. L. Dudarev, G. A. Botton, S. Y. Savrasov, C. J. Humphreys, and A. P. Sutton. Electron-energy-loss spectra and the structural stability of nickel oxide:an LSDA+U study. *Phys. Rev. B*, 57:1505–1509, 1998.

[67] N. Orita. Generalized gradient approximation +U study for metallization mechanism of niobium-doped anatase titanium dioxide. *Jpn. J. Appl. Phys.*, 49:055801, 2010.

[68] J. Heyd, G. E. Scuseria, and M. Ernzerhof. Hybrid functionals based on a screened coulomb potential. *J. Chem. Phys.*, 118(18):8207–8215, 2003.

[69] J. Heyd, G. E. Scuseria, and M. Ernzerhof. Erratum: Hybrid functionals based on a screened Coulomb potential. *J. Chem. Phys.*, 124:219906, 2006.

[70] P. Deák, B. Aradi, and Th. Frauenheim. Polaronic effects in $TiO_2$. *Phys. Rev. B*, 83:155207, 2011.

[71] H. Hellmann. A new approximation method in the problem of many electrons. *J. Chem. Phys.*, 3:61, 1935.

[72] C. Herring. A new method for calculating wave functions in crystals. *Phys. Rev.*, 57:1169–1177, 1940.

[73] P. E. Blöchl. Projector augmented-wave method. *Phys. Rev. B*, 50(24):17953–17979, 1994.

[74] G. Kresse and D. Joubert. From ultrasoft pseudopotentials to the projector augmented-wave method. *Phys. Rev. B*, 59(3):1758–1775, 1999.

[75] O. K. Andersen. Linear methods in band theory. *Phys. Rev. B*, 12:3060–3083, 1975.

[76] G. Kresse and J. Hafner. Ab initio molecular-dynamics simulation of the liquid-metalamorphous-semiconductor transition in germanium. *Phys. Rev. B.*, 49:14251–14269, 1994.

[77] G. Kresse and J. Furthmuller. Efficient iterative schemes for ab initio total-energy calculations using a plane-wave basis set. *J. Phys. Rev. B*, 54:11169–11186, 1996.

[78] *VASP code http://www.vasp.at/.*

[79] D. Porezag, Th. Frauenheim, Th. Köhler, G. Seifert, and R. Kaschner. Construction of tight-binding-like potentials on the basis of density-functional theory: Application to carbon. *Phys. Rev. B*, 51:12947–12957, 1995.

[80] M. Elstner, D. Porezag, G. Jungnickel, J. Elsner, M. Haugk, Th. Frauenheim, S. Suhai, and G. Seifert. Self-consistent-charge density-functional tight-binding method for simulations of complex materials properties. *Phys. Rev. B*, 58:7260, 1998.

[81] B. Aradi, B. Hourahine, and Th. Frauenheim. DFTB+, a sparse matrix-based implementation of the DFTB method. *J. Phys. Chem. A*, 111:5678–5684, 2007.

[82] Jenő Sólyom. *Fundamentals of the Physics of Solids.* Springer, 2010.

[83] H. J. Monkhorst and J. D. Pack. Special points for brillouin-zone integrations. *Phys. Rev. B*, 13(12):5188–5192, 1976.

[84] J. Muscat, V. Swamy, and N. M. Harrison. First-principles calculations of the phase stability of $TiO_2$. *Phys. Rev. B*, 65:224112, 2002.

[85] A. V. Emeline, Y. Furubayashi, X. Zhang, M. Jin, T. Murakami, and A. Fujishima. Photoelectrochemical behavior of Nb-doped $TiO_2$ electrodes. *J. Phys. Chem. B*, 109(51):24441–24444, 2005.

[86] C. G. Van de Walle and J. Neugebauer. First-principles calculations for defects and impurities: Applications to III-nitrides. *J. Appl. Phys.*, 95:3853–3879, 2004.

[87] J. Spyridelis, P. Delavignette, and S. Amelincks. On the superstructures of $Ta_2O_5$ and $Nb_2O_5$. *Phys. Stat. Sol.*, 19:683–704, 1967.

[88] H. Xu, D. Lee, J. He, S. B. Sinnott, V. Gopalan, V. Dierolf, and S. R. Phillpot. Stability of intrinsic defects and defect clusters in $LiNbO_3$ from density functional theory calculations. *Phys. Rev. B*, 78:174103, 2008.

[89] A. Fukumoto and K. Miwa. Predic of hexagonal $Ta_2O_5$ structure by the first-principles calculations. *Phys. Rev. B*, 55:11155, 1997.

[90] L.A. Aleshina and S.V. Loginova. Rietveld analysis of X-ray diffraction pattern from $\beta$-$Ta_2O_5$ oxide. *Crystall. Rep.*, 47:460, 2002.

[91] B. R. Sahu and L. Kleinman. Theoretical study of structural and electronic properties of $\beta$-$Ta_2O_5$ and $\delta$-$Ta_2O_5$. *Phys. Rev. B*, 69:165202, 2004.

[92] D. R. Lide. *CRC Handbook of Chemistry and Physics*. CRC Press, 2009.

[93] U. Diebold. The surface science of titanium oxide. *Surf. Sci. Rep.*, 48:53–229, 2003.

[94] M. Ramamoorthy and D. Vanderbilt. First-principles calculations of the energetics of stoichiometric $TiO_2$ surfaces. *Phys. Rev. B*, 49:16721–16727, 1994.

[95] M. Lazzeri, A. Vittadini, and A. Selloni. Structure and energetics of stoichiometric $TiO_2$ anatase surfaces. *Phys. Rev. B*, 63:155409, 2001.

[96] T. X. T. Sayle, C. R. A. Catlowa, D. C. Sayleb, S. C. Parkerb, and J. H. Harding. Computer simulation of thin film heteroepitaxial ceramic interfaces using a near-coincidence-site lattice theory. *Philos. Mag. A*, 68:565–573, 1993.

[97] C. A. J. Fisher and H. Matsubara. Molecular dynamics simulations of interfaces between NiO and cubic $ZrO_2$. *Philos. Mag*, 85:1067–1088, 2005.

[98] N. A. Deskins, S. Kerisit, K. M. Rosso, and M. Dupuis. Molecular dynamics characterization of rutile-anatase interfaces. *J. Phys. Chem.*, 111:9290–9298, 2007.

[99] *DFTB+ code http://www.dftb-plus.info/.*

[100] T. Tanaka, K. Teramura, T. Yamamoto, S. Takenaka, S. Yoshida, and T. Funabiki. $TiO_2/SiO_2$ photocatalysts at low levels of loading: preparation, structure and photocatalysis. *J. Photochem. Photobio A: Chem.*, 148:277–281, 2002.

[101] C. G. Van de Walle and R. M. Martin. Theoretical calculations of heterojunction discontinuities in the Si/Ge system. *Phys. Rev. B*, 34:5621–5634, 1986.

[102] P. Deák, B Aradi, and T. Frauenheim. Polaronic effects in $TiO_2$ calculated by the HSE06 hybrid functional: Dopant passivation by carrier self-trapping,. *Phys. Rev. B*, 83:155207, 2011.